ICRF Heating Analysis on ASDEX Plasmas

S.-I. Itoh*, K. Itoh**, A. Fukuyama***,
T. Morishita***, K. Steinmetz, J.-M. Noterdaeme,

IPP III/115 August 1987

MAX-PLANCK-INSTITUT FÜR PLASMAPHYSIK

8046 GARCHING BEI MÜNCHEN

MAX-PLANCK-INSTITUT FÜR PLASMAPHYSIK

GARCHING BEI MÜNCHEN

ICRF Heating Analysis on ASDEX Plasmas

S.-I. Itoh*, K. Itoh**, A. Fukuyama***,
T. Morishita***, K. Steinmetz, J.-M. Noterdaeme,

IPP III/115 August 1987

* Institute for Fusion Theory, Hiroshima Univ., Hiroshima 730, JAPAN
** Plasma Physics Laboratory, Kyoto Univ., Uji 611, JAPAN
*** School of Engineering, Okayama Univ., Okayama 700, JAPAN

Die nachstehende Arbeit wurde im Rahmen des Vertrages zwischen dem Max-Planck-Institut für Plasmaphysik und der Europäischen Atomgemeinschaft über die Zusammenarbeit auf dem Gebiete der Plasmaphysik durchgeführt.

Abstract

ICRF (ion cyclotron range of frequencies) waves heating in ASDEX tokamak is analysed. The excitation, propagation and absorption are studied by using a global wave code. This analysis is combined with a Fokker-Planck code, and the generation of fast ions and thermalization of the absorbed power are obtained theoretically. The wave form in the plasma, the loading resistiance and reactance of the antenna are calcualted for both the minority ion heating and the second harmonic resonance heating. Attention is given to the change of the antenna loading associated with the L/H transition. Optimum conditions for the loading are discussed. In the minority heating case, the tail generation and thermalization are analyzed. Spatial profiles of the tail-ion temperature and the power transferred to the bulk electrons and ions are obtained. Central as well as off-central heating cases are investigated. The ratio of the electron heating power is obtained. Finally, the effect of the reactive electric field is discussed in connection with rf losses and impurity production.

§I. Introduction

ICRF heating schemes have been considered as a major tool to heat in toroidal experiments. Recently, several MW of ICRF wave power have been launched in the plasma chamber. To explain experimental results and to have a perspective to the future parameters, a comprehensive study is necessary. To this end we have been exploiting analytical method and the computer codes. In order to analyze an ICRF heating process, we divide it into three phases according to the different time scales. Namely, 1) the wave absorption phase which includes excitation, propagation and absorption of the wave; 2) the velocity relaxation phase where the modification of a velocity distribution is due to the balance between absorption and collisional relaxation; and 3) is the transport phase where the wave energy is redistributed in real space. The typical time scales of these phases are 1) a/v_g: the plasma radius divided by the group velocity of the launched wave, 2) ν^{-1}: the collisional relaxation time, and 3) τ_E: the energy confinement time.

In analyses of the first stage, there are two methods to describe the wave propagation and absorption. One is the ray-tracing method (based on the geometrical optics)[1,2] and the other is to solve the wave equation directly[3-5]. The ray tracing has been applied to ASDEX to predict the basic feature of the wave propagation[6]. In this report, we apply the latter method[3], which can reveal the coherent structure of the wave characteristics and the global coupling to the antenna. This method has been successfully applied to explain the global quantities of the experimental results in various tokamaks[7-10]. The wave calculation includes kinetic effects, such as the wave-particle interaction and the finite gyroradius effect up to the 2nd order.

The global wave code is connected to the isotropic Fokker-Planck equation with a quasi-linear diffusion[11,12]. This extension enables us to calculate the modification of the velocity space due to the ICRF heating. The combined analysis of the phases (1) and (2) explores the time developments of the wave field structure and global coupling in accordance with the relaxation processes. The energy transport in a real space is not yet taken into account. Both the minority heating scheme and the 2nd harmonic heating scheme are examined for ASDEX plasma parameters.

In the minority heating case, most of the wave power is absorbed by minority ions through fundamental cyclotron damping. The high energy tail component is formed in the vicinity of the resonance layer. These fast ions collide with bulk electrons as well as majority ions and transfer the energy to them. The scheme has been predicted and analyzed in a local approximation for a given wave-field by Stix[11]. Our analysis extends his theory to a nonlocal theory using a directly obtained wave-field structure. We calculate the localization of the high energy ions with their maximum energy in an inhomogeneous plasma.

The outline of this report is the following. In §2, we briefly present our basic equations and the theoretical model. We discuss the important physics quantities, which can be computed from our codes. The simulation results for ASDEX experiments are shown in §3 and 4. In §3, the coupling studies of two heating schemes, i.e., minority heating and the 2nd harmonic heating, are presented. We also examine the difference of the loading resistance between L-mode and H-mode discharges. §4 is devoted to topics related to the fast-ion generation in the case of the minority heating. The temporal evolution and the power scan of related quantities are obtained. In §5, the effect of the ICRF launching to the plasma in a peripheral region is discussed based upon the numerical results obtained in §3. The role of the reactive electric field near the antenna is considered in relation to the impurity release and the impurity influx. The direct loss of the wave to the divertor region (which does not couple to the main plasma) is also discussed. In the final section, a brief summary and discussions are given.

§2 Basic Equations and Theoretical Model

For the analyses of the wave field structure, we formulate the basic equation as a boundary value problem. The basic equation governing the propagation and absorption of the wave has been reported in refs. /3, 4, 13/. Here we adopt the one-dimensional stratified model plasma in a strong magnetic field along the Z-axis, i.e. $B(x)=B_o/(1+x/R)$. The plasma is assumed to be uniform in the Y and Z directions. The plasma is composed by the majority deuterons, n_D, the minority proton, n_H, and electrons for the case of the minority heating. (n_H and electrons for the 2nd harmonic case).

The initial density and temperature profiles of electrons and ions are simulated by the experimental observations as[14,15]

$$n_j(\chi) = \begin{cases} (n_{jo} - n_{js})(1-x^2/a_s^2) + n_{js} & /x/ \leqq a_s \\ n_{js}\exp\{-(/x/-a_s)/\lambda_n\} & a_s \leqq /x/ \leqq a_L \end{cases} \quad (1)$$

$$T_j(\chi) = \begin{cases} (T_{jo} - T_{js})(1-x^2/a_s^2) + T_{js} & /x/ \leqq a_s \\ T_{js}\exp\{-(/x/-a_s)/\lambda_T\} & a_s \leqq /x/ \leqq a_L \end{cases}$$

where the suffix j stands for the particle species. We introduce the density and temperature fall-off lengths λ_n and λ_T in order to simulate the scrape-off layer. Notations a_s and a_L mean the separatrix radius and the location of the guard limiter of an antenna as illustrated in Fig. 1. The plasma in scrape-off layer extends to the guard limiter. Outside of the radius of the guard limiter, $/x/>a_L$ is assumed to be vacuum. In the initial state, we assume that the minority ion distribution has the same profile as that of the bulk ions and that there is no high energy ion tail component, i.e., $n_t(x) = 0$.

A model antenna is located at x=d, which corresponds to the location of the central conductor, in a low field side, and carries the sheet current in the Y direction as

$$J^A = \sum_{k_z} J(k_z)\delta(x-d)\exp(ik_z z - i\omega t) \quad (2)$$

where J(z) is fourier decomposed as, $J(z)=\sum_k J(k_z) \cdot \exp(ik_z z)$. We choose (for simplicity) the current distribution in Z-direction $J^A(z) = \exp\{-4z^2/L_T^2\}$ to simulate the full toroidal width of the antenna to be L_T. The wall is located at x=±b. Figure 1 shows the schematic configuration of the model geometry.

The wave equation inside the plasma is

$$\nabla x \nabla x \vec{E} - \omega^2/c^2 \vec{E} = i\omega\mu_o(\sum J_j) \quad (3)$$

where J_j is the oscillating current of j-th species (j=e, H_t, H_b, D). In order to include the plasma inhomogeneity and the wave dispersive effect, we use the collisionless conductivity tensor[3] as

$$J_{pq}(x) = \sum_q [\, \sigma^{(0)}_{pq}(x)E_q(r) - i\{\sigma^{(1)}_{pq}(x)\frac{\partial E_q(r)}{\partial x} + \frac{1}{2}\frac{\partial \sigma^{(1)}_{pq}(x)}{\partial x}E_q(r)\} - \frac{1}{2}\{\sigma^{(2)}_{pq}(x)\frac{\partial^2 E_q(r)}{\partial x^2} + \frac{\partial \sigma^{(2)}_{pq}(x)}{\partial x}\frac{\partial E_q(r)}{\partial x} + \frac{1}{4}\frac{\partial^2 \sigma^{(2)}_{pq}(x)}{\partial x^2}E_q(r)\}\,] \tag{4}$$

where $\sigma=\sigma^{(0)} + \sigma^{(1)}k_x + (1/2)\sigma^{(2)}k_x^2$ and p and q stand for x,y and z. We have assumed that an inhomogeneity of the equilibrium configuration is weak compared with the gyroradius and have retained the second-order dispersive effects in order to describe the mode conversion to the ion Bernstein wave near the second cyclotron harmonic. Within the framework of our analysis the Poynting theorem $\nabla\cdot\vec{S}+\sum\langle\vec{J}_j\cdot\vec{E}\rangle=0$ is satisfied, where $P_j(\vec{r}) = \langle\vec{J}_j\cdot\vec{E}\rangle$ is the power density absorbed by j-th species. The symbol $\langle\rangle$ shows the time average over the wave period.

Directly computing Eq.(3) with Eq.(4) for appropriate launching conditions of antennae and for the plasma pressure profiles, we obtain the wave field structure, $\vec{E}(\vec{r})$, the spatial deposition profile to each species, $P_j(\vec{r})$, the power partition of the absorbed power, $\int P_j(\vec{r})d\vec{r} = P_j$, and the absorption spectra which can be compared with the radiation spectra from the antenna. Since we calculate the power deposition for a given antenna current, $I_A=\int_{-L_T/2}^{L_T/2} J(z)dz$, the total absorption of the plasma, $P_{abs}=\int\sum_j P_j(\vec{r})d\vec{r}$ (summed up over each plasma species and integrated over the plasma column) has the relation to the loading resistance, $\hat{R}$, as

$$(1/2)\hat{R}\, I_A^2 = P_{abs} + \bar{P}_{NON} \tag{5}$$

where $\bar{P}_{NON}$ denotes the power which is radiated from the antenna but is not absorbed by the main plasma. Example of the nonplasma power loss, $\bar{P}_{NON}$, may be attributed to the power dissipated on the wall (due to the finite resistivity), to the direct loss of escaped wave power from the chamber through the ports and so on. We first assume that $\bar{P}_{NON}=0$ for simplicity. Since, if we include the power loss on the wall (stainless steel case), the loss power is calculated to be small (order of 10^{-3}) as compared with the absorption power.

As a global response function of the antenna current, we obtain the loading impedance, $\hat{Z} = \hat{R}-i\hat{X}$, where $\hat{X}$ is the reactance of the antenna. The reactance does not contriubte to the absorption, but it plays an important role for obtaining the optimum loading condition. The reactive electric field may also affect the ion acceleration (accordingly, the enhancement of the impurity influx) in front of the antenna. In the one dimensional calculation, the antenna impedance per unit arc length, $\hat{Z}$, is obtained. Multiplying the arclength L_A, we have the antenna impedance, $\hat{Z}=\hat{Z}L_A$. From the results of 2D calculations, we have found that this estimation of resistance is accurate enough and that the value of $\hat{X}$ can change from this evaluation due to the effect of the feeders (this change is of the order unity).

The calculated absorptions tell us how much of the power is going to electrons, minority ions and the majority ions (bulk). In the heating scheme of the minority heating, the major part of the absorbed power goes to minority ions at the cyclotron fundamental resonance. Its power strongly modifies the minority velocity distribution. We combine the Fokker-Planck equation on each magnetic surface in the following manner. In the isotropic approximation, we employ the Fokker-Planck Equation for minority species as[4)]

$$\frac{\partial f}{\partial t} = \frac{1}{v^2}\frac{\partial}{\partial v}\left[-\alpha v^2 f+\frac{1}{2}\frac{\partial}{\partial v}(\beta v^2 f) + Kv^2\frac{\partial f}{\partial v}\right] \tag{6}$$

where α and β stand for the Coulomb colision term with bulk particles. The rf heating term, K, is deduced by averaging the quasi-linear diffusion term over the magnetic surface in tokamaks:

$$\alpha \equiv \langle \Delta v_{\shortparallel} \rangle + \frac{1}{2v}\langle (\Delta v_{\perp})^2 \rangle \qquad \langle \Delta v_{\shortparallel} \rangle = -\sum_f C_f \ell_f^2 \left(1+\frac{m}{m_f}\right) G(\ell_f v)$$

$$\beta \equiv \langle (\Delta v_{\shortparallel})^2 \rangle \qquad \langle (\Delta v_{\shortparallel})^2 \rangle = \sum_f \frac{C_f}{v} G(\ell_f v) \tag{6'}$$

$$K \equiv \frac{\langle P \rangle}{3 n_i m_i} \qquad \langle (\Delta v_{\perp})^2 \rangle = \sum_f \frac{C_f}{v}\left[\Phi(\ell_f v) - G(\ell_f v)\right]$$

where

$$C_f = \frac{2n_f Z_f Z^2 e^4 \ln\Lambda}{\varepsilon_0 m^2}$$

$$\ell_f{}^2 = m_f / 2T_f$$

$$\Phi(x) = \frac{2}{\pi^{1/2}} \int_0^x \exp(-y^2)\, dy$$

$$G(x) = \frac{\Phi(x) - x\Phi'(x)}{2x^2}$$

<P> is an absorbed power density averaged over the magnetic surface, and m, Z, n, T and v are the mass, the charge number, the number density, the temperature and the velocity of the test particles (minority ions), respectively. We use the subscript f to designate the background plasma particles, i.e., e for electrons and i for majority ions. Note that $_{\parallel}$ and $_{\perp}$ denote directions with respect to the velocity of the test particle $\vec{v}$ and not with respect to $\vec{B}$.

To have an insight, let us show the approximate steady state, the isotropic solution of Eq.(6) for the minority species[11],

$$\ln f(v) = -\frac{E}{T_e(1+\xi)} \left[1 + \frac{R_i(T_e - T_i + \xi T_e)}{T_i(1+R_i+\xi)} H(E/E_i)\right] \qquad (7)$$

where

$$E = \frac{mv^2}{2} \qquad \xi \equiv \frac{2K}{\varepsilon C_e \ell_e}$$

$$\varepsilon \equiv \frac{2}{3\pi^{1/2}} \qquad E_i(\xi) = \frac{mT_i}{m_i} \left(\frac{1+R_i+\xi}{2\varepsilon(1+\xi)} \right)^{2/3}$$

$$R_i \equiv \frac{n_i Z_i^2 \ell_i}{n_e \ell_e} \qquad H(x) \equiv \frac{1}{x} \int_0^x \frac{du}{1+u^{3/2}}$$

This approximate solution (7) has been reported[11,16] to agree with the direct numerical calculation, provided that the pulse length of the input

power and the spatial transport time are long enough compared with the electron-ion collision time, τ_{ie}. In this report, we solve Eq.(6) directly to obtain the distribution of the minority, $f_H(v)$. When we obtain the distribution, the power transferred to bulk electrons, P_{ec}, and to the bulk ions, P_{ic}, from the hot component of the minority hydrogen through collisions are obtained by

$$P_{ec} = \frac{m\varepsilon C_e \ell_e}{\varepsilon_0 \ell_i^3} \int_0^\infty u\left[\left(\frac{mT_i}{m_i T_e} u - \frac{1}{u} \right) u^2 f + \frac{1}{2} \frac{\partial}{\partial u} u^2 f \right] du \tag{8}$$

$$P_{ic} = \frac{m\varepsilon C_e \ell_e}{\varepsilon_0 \ell_i^3} \frac{C_i \ell_i}{C_e \ell_e} \int_0^\infty \frac{u}{1+2\varepsilon u^3} \left[\left(\frac{m}{m_i} u - \frac{1}{u} \right) u^2 f + \frac{1}{2} \frac{\partial}{\partial u} u^2 f \right] du$$

where $u = l_i v$. The RF power absorbed by minority ions is given by

$$P_{minority} = - \frac{m\varepsilon C_e l_e}{\varepsilon_0 l_i^3} \xi \int_0^\infty u\left[-1/u(u^2 f) + 1/2 \; \partial/\partial u(u^2 f) \right] du \tag{9}$$

and is proportional to ξ. In a steady state, the power conservation law $P_{minority} = P_{ec} + P_{ic}$ holds.

We notice the importance of the parameter ξ (so-called Stix's ξ parameter), which is basically the ratio of the local heating time, $\tau_h \equiv \langle P \rangle / 3nT_e$, and the local cooling time due to electron collisions, τ_{ie}. Therefore, in a steady state the temperature of the hot component of the minority reaches $T_e(1+\xi)$ in the absence of other losses.

The tasks casted to us are how we combine the wave deposition profile, $P_j(r)$, and obtain the absolute value of ξ as well as its spatial profile $\xi(\vec{r})$ in a consistent manner. The power deposition profile obtained by 1D kinetic wave-code is calculated on the X-axis (mid plane), which is transformed to the power deposition on each magnetic surface, $\langle P \rangle$, in the following way. We assume that the deposition in the y-direction is localized with a parabolic profile in the area $-L_y/2 < y < L_y/2$, where L_y is the length of the deposition in the poloidal direction. Owing to the focusing effect of the fast wave to the high density region, L_y is chosen to be smaller than the poloidal arc length of the antenna L_A. Here we

choose $P_j(y) \propto (1-(2y/L_y)^2)$. This assumption is made by the comparison analysis with the results of 2D kinetic code[4,9]. From this assumption we obtain <P> as a function of the minor radius r. Using thus transformed deposition profile, we solve the Fokker-Planck equation and calculate ξ and other parameters. The numerical scheme is shown in Fig. 2. We repeat calculations of the wave equation and Fokker-Planck equation following the temporal evolution of f(v), until the physical quantities reach the stationary state. This calculation shows us not only the effective temperature of the ICRF produced fast ions but also their localization profile in real space. Simultaneously, we can see how the input power, which is first deposited to minority ions, distributes to electrons and ions.

§3 Coupling Study

In this section we apply our analyses on the wave coupling to ASDEX plasmas. The standard parameters we use are summarized in table 1. The wave code analyses are made for both the minority heating scheme and the 2nd harmonic heating scheme.

3.1 Minority heating

We first examine the minority heating case where the minority hydrogen (H) of 5% is mixed in the majority deuterons (D). The concentration ratio, $\eta \equiv n_H/n_e$ is 0.05. Figure 3 shows the wave propagation and absorption structure in the radial direction on the Z=0 plane (3(a):E_x, 3(b):E_y). The fast wave (mainly E_y component) is launched at the low-field-side antenna and propagates into the plasma. A part of the fast wave is mode-converted to Ion Bernstein mode of short wave length as seen in a high-field-side of Fig. 3(b). Figure 3(c) depicts the direct power absorption profile of the minority protons, $\int P_H(r)dz$, that of the deuterons, $\int P_D(r)dz$, and that of the electrons, $\int P_e(r)dz$. The total absorption profile, $\int P_{tot}(r)dz$, and the Poynting flux, $\int S_x(r)dz$, are also shown. The deposition profiles are integrated along the Z-direction, namely 128 modes with respect to k_z are summed up. We see that the major part of the wave energy is absorbed by the minority protons near the fundamental cyclotron resonance region as shown in Fig. 3(c). A small fraction of the wave energy is absorbed either by majority deutrons by the 2nd harmonic resonance or by electrons through Landau damping (higher field side).

With respect to the absorption spectra, we plot the power absorbed (integrated over the minor radius) by each k_z mode in Fig. 4. The distribution among different species are also plotted. Several peaks are due to the cavity eigenmode effect. (The results by 1D model code shows the stronger cavity effect, if we compare with those obtained by 2D model calculation[4].) The sharp decrease of the coupling in higher $k_{\parallel}(k_z)$ side is originated from the wave accessibility condition, i.e.,

$$/k_{\parallel}/ < /k_{\parallel c}/$$
$$k_{\parallel c}{}^3 \simeq \left[\omega_{PD}^2/c^2 \cdot (dn/dr)/n\right]_r \simeq a_L \qquad (10)$$

For the large $k_{\parallel}$ component, the evanescent region is too thick to access the main plasma region. The zero $k_{\parallel}$ mode is hardly absorbed because little particle satisfies the resonance condition with the wave.

In the case of minority heating (33.5 MHz), the resistance of a half antenna ($L_A/2$ = 0.39 m) is calculated to be ($d-a_L$=2.6 m) around 2.7 Ω. The observed value is around 2.7 Ω. The agreement is within error bars of both in experiment and in a theoretical model. It should be noted that the value of the calculated resistance changes according to the plasma boundary conditions as well as to the distance between the plasma and the antenna. These changes are also observed experimentally. Furthermore, in ASDEX experiment, it is observed that the sudden change in the loading resistance occurs when the plasma does L→H transition[7]. (Typically from 2.7 Ω(L-phase) to 1.8 Ω(H phase).

In order to analyze these behaviours, we examine the loading resistance by changing the conditions of, i.e., 1) the density and the temperature fall-off lengths, λ_n and λ_T, from 0.5 cm to 10 cm, 2) the scrape-off density itself, n_{js}, 3) the distance between the central conductor and the guard limiter of the antenna $d-a_L$, and 4) the distance between the central conductor and the separatrix radius $d-a_s$. The results are plotted in Fig. 5 for full antenna, L_A=0.78 m. For fixed values of d, a_L and n_{js}, say $d-a_L$=2 cm, the loading decreases from around 7Ω to ~4.8Ω (I, III) as λ_n and λ_T decrease. The reduction rate may reach more than 30% as seen in Fig. 5. A similar curve of the resistance R is obtained when we decrease the scrape-off density, n_{js}, for fixed value of $d-a_L$=2 cm. The decrease of n_{js} usually reduces the loading. The result in Fig. 5 differs from the general depen-

dence on n_{js}, since the effect of the cavity eigenmode is stronger than the effect of the change in the scrape off density. More dramatical changes are observed when the distance between the antenna and the plasma surface becomes large.

When we increase the distance between the separatrix radius and the guard limiter of the antenna, a_L-a_s, for the fixed fall-off lengths, the loading resistance reduces more than 30% as is shown in Fig. 5 (II). A particular case is examined for d-a_L=2.6 m, $\lambda_{n,T}$=2 cm, simulating the L→H transition which is mentioned above. The charge in a_L-a_s from 3cm to 5cm causes the change in loading resistance from 2.7Ω to 1.9Ω. A similar effect is seen when we change the distance between the central conductor of the antenna and the guard limiter. Only 1 cm change in the distance causes the reduction of more than 30% (from d-a_L=2 cm to d-a_L=3 cm) in the loading resistance (IV). Therefore we may say that the distance between the central conductor of the antenna and the plasma surface dictates the loading resistance of the antenna.

The transition from L to H in experiments may involve the effects above. Namely, the enlargement of the distance a_L-a_s, the decreases of the density and the temperature fall-off lengths and the reduction of n_{js} appear simultaneously. Even though their mixture may not be discriminated we may say that we have a fairly good explanation to the experimentally observed values.

In order to study the coupling of the antenna to the plasma, we calculate the total impedance, $\hat{Z}$. The loading reactance and the resistance are plotted v.s. the effective antenna width in toroidal direction, L_T, (Fig. 6). The calculation confirms the optimum coupling condition to present ASDEX parameters. Namely, the high value of $\hat{R}$ at low value of $\hat{X}$ is found at around $L_T \simeq$ 18 cm, which is the value of the ASDEX launching system.

It is well known that the effective toroidal extent, L_T, can be controlled by using the phase control of antenna array. There is a possibility to compensate for the sudden change of the $\hat{R}$ during the L→H(H→L) transition, if a fast feedback control in phasing between antennas could be done, provided that the maximum electric field, E_{max}, can be made high. The crude way is to start the launching with a non-optimum (low loading) condition in order to have a margin to an optimum loading (the case for L→H).

3.2 2nd Harmonic Heating

The 2nd harmonic heating case, Ω_{2H}: $\omega/2\pi$=67 MHz for the pure hydrogen plasma, is studied in the same framework as of the minority case (3.1). The wave structure is obtained to be qualitatively similar to those in Fig. 3. (The wavelength becomes shorter due to the high frequency.) The absorption is mainly due to the 2nd harmonic resonance of hydrogen. The difference is seen in the absorption spectra. The spectra in Fig. 7 (for 2nd harmonic heating) can be compared to those in Fig. 4. The $k_{\parallel}$ cut-off is higher according to the increase of the frequency: The wave becomes less evanescent for the higher frequency. Therefore the larger $k_{\parallel}$ modes are accessible to the core plasma and absorbed. Also seen are the peaks of the absorption due to the cavity eigenmode effect. The absorption to electrons is also plotted. This is found to be small (<~8%).

The dependence of the loading resistance on the density and the temperature fall-off-lengths is studied in Fig. 8. The cases of $n_{se}=10^{19}$ m^{-3}; d-a_L=2 cm and d-a_L=3 cm are studied. A stronger dependence of $\hat{R}$ on λ_n and λ_T is found, if the result is compared to that in Fig. 5. This is expected because the density at the fast wave cut-off near the surface is lower in the 2nd cyclotron resonance heating than in the case of the minority heating. Due to this difference, the change of λ_n is more effective to change the position of the cut-off layer in the case of the 2nd harmonic heating than in the case of the minority heating. The dotted lines in Fig. 8 are for the case that the antenna is far: a_L-a_s=5 cm.

To complete the analysis of the wave-field (which corresponds to the structure at the onset of the launching), let us show the peripheral data of the wave-field associated with launching. In Fig. 9, we show the E_y component (solid line - real part, dashed line - imaginary part) of the field in the toroidal direction on the surface of the antenna position (r=d). The minority case is plotted in Fig. 9(a) and 2nd harmonic case is in Fig. 9(b). In the case of the minority heating, the wave field falls off by an order of magnitude within the length $\pm\Delta Z \approx 0.5$ m in the toroidal direction. This value can be roughly estimated by taking $\Delta Z \simeq \pi/k_{\parallel c}$. This result shows the similar dependence of JET ICRF launching condition[8, 9]. The absolute value of the wave field strength is evaluated at I_A=1A, that is, at the power level of 6W.

The case of the 2nd harmonic heating shows a different structure in the Z-direction as shown in Fig. 9(b). The strong fall-off of the wave field is not seen due to the remaining cavity component as is illustrated in Fig. 7. The finite E_y component of a few V/m at the power level of $\leq$10 W (I_A = 1A) remains over the toroidal extent. This electric field may affect the peripheral and boundary conditions of the plasma in an intense heating case. Some discussions are made in §5.

§4 Temporal Evolution of Heating Process and Fast Ion Generation

Following the model described in §2, we proceed to the heating analysis with respect to the minority heating scheme. The solution of the wave-equation gives us the aspect of the coupling condition and the wave-field structures. However, the result in §3 is restricted to the linear analysis and to the time scale which is short compared with the relaxation times. The analysis in this section shows the time evolution of the heating process as well as the input power dependences of observation variables.

Firstly, we simulate the central deposition case, where the cyclotron resonance region is located near the plasma center. As shown in the preceding section, the major part of the rf power is absorbed by protons. Electrons and deuterons are heated by rf generated fast protons. Therefore, the power partition depends on the evolution of the kinetic energy of fast ions. In calculating the time evolution, we choose L_y=40 cm. The calculation based on the 2D wave form has confirmed that this choice of the length is little affected by the high energy ion generation[12, 18]. Figure 10 shows the time evolution of the volume-integrated power inputs to electrons (dashed line) and ions (solid line), which are obtained by the combination of the isotropic Fokker-Planck calculation with Eqs. (8) and (9) and wave calculation. Direct absorptions (P_{ed}, P_{Dd}) are also included. The total power is kept constant to be about 0.15 MW. The power transferred to ions reaches up to 70% of the steady state value after about 2 msec, but that to electrons increases more than 20 msec (which corresponds to the time for the ion tail formation becomes steady state).

The power deposition profiles (heating profiles) and the profile of the effective temperature of fast ions, T_h, at the steady state are shown in Fig. 11(a) and (b). The different cases of the power input are shown in

(a): P_{rf} ~ 0.16 MW and in (b) P_{rf} ~0.31 MW. We see that the generation of the fast ions and the heating of the bulk plasma occur in the plasma core region. The maximum kinetic energy and the half width at half maximum of the T_h profile are larger for the case (b). In order to reach the quasi-steady state, it takes about 50 msec in the case (b). Even for the case of the higher power level of 1 MW, the high energy particle generation is localized to the central core region $r \lesssim a/4$.

The change in power input, however, causes the change in partition ratio of P_{Dc} and P_{ec}. The partiction ratios are plotted in Fig. 12. P_{ed}, P_{ec}, P_{Dc} and P_{Dd} denote the direct rf absorption by electrons, the power transferred from fast ions to electrons, that transferred to majority ions and the direct rf absorption by deuterons, respectively (: all are volume-integrated values). As the power increases, the total power input to electrons becomes larger. It may reach more than 60% at the power level of 0.6 MW.

Tail generation affects not only the spatial deposition profiles (Fig. 11) but also the rf absorption spectra. The change of $k_{\parallel}$-spectrum of the power absorption is shown in Fig. 13. The dashed line shows the initial spectrum (onset of the ICRF wave) and the solid line is the case for t=100 ms after the rf injection ($P_{rf} \simeq 0.3$ MW). The graph clearly shows the broadening of the absorption spectra which is caused by the high energy fast ions. Within a framework of 1D code calculation the width of the absorption layer in x-direction, Δ_x, is estimated to be $\Delta_x \simeq 3Rk_{\parallel} v_{Tf}/\Omega_H$ where v_{Tf} is the thermal velocity of fast ions. If Δ_x exceeds the wave length and $k\Delta_x \gtrsim 1$, then the resonant cavity modes are suppressed. With respect to the cavity effect, we previously compared the results of 1D code and those of 2D code. The typical cavity eigenmode effect is suppressed by a factor of 10 if we employ 2D code. The case was done for JT-60 and was compared with the experimental observation of the appearance[19]. The density scan of the loading resistance in experiment has shown the presence of eigenmode which agrees with our calculation, however, their magnitude is slightly less than the 2D code prediction. (O(10) times less than the 1D code calculation.)

Figure 11 shows that the maximum temperature of the fast ions increases as the power increases. The power scan is shown in Fig. 14(a) for fixed concentration ratio of minority ions. The solid line shows the

central deposition case. This indicates that at the power level of 0.5 MW T_h^{max} reaches to 50 keV in the central core region. The dashed line shows the case of the off-central deposition as will be discussed later. For a fixed power level, a scan over the minority concentration ratio, $\eta' \equiv n_H/n_D$, is plotted in Fig. 14(b). As the value of η' increases, the number of the minority ions which absorb the wave increases; then the maximum kinetic energy of fast ions decreases.

The central deposition of the wave predicts the electron heating through the fast ions in the core region. The increase of T_e inside the q=1 surface may affect the MHD stability. The study on the MHD stability of the ICRF-heated plasma shows that the strong central heating can violate the m=n=1 ideal pressure-driven kink stability condition[18]. With regard to this, the off-centered deposition should be investigated in more detail.

Next we examine the off-central deposition case. Figure 15 depicts the effective temperature of the fast ions, T_h, heating power to electrons (P_{et}: total value) and that to deuterons, P_{Dt}, in the case where the resonance surface is located at r/a_s=0.37 (B_o=2.4 T). Comparing the result to that in Fig. 11, the shifts of peaks as well as the reductions of the absolute values are seen. The maximum value of T_h decreases to 20 keV instead of 40 keV in Fig. 11(a). The temporal evolution of the power partition ratio also changes in the case of the off-centered heating (Fig. 16). In this case, it takes about 40 msec in order that the partition reaches the quasi-steady state. Also shown is the power scan of the power partition ratio in Fig. 17: The power to electrons increases when the power input increases, as in the case of the central heating case (in Fig. 14). A difference is, however, found in the reduction of the electron heating rate at fixed power. For a given power, the maximum kinetic energy of fast ions becomes lower in the case of off-central heating, since the deposition area is larger. Electron heating rate reduces. However at the power level of 1.2 MW, the electron heating rate reaches 70% of the total rf power input.

Before closing this section, let us discuss the role of fast-ions due to NBI heating. Neutral beam injection generally makes the high energy ion tail of several 10 keV. It has been suggested that this helps for the ICRF waves to be absorbed inside the plasma[20]. The difference is noticable in the case of the 2nd harmonic heating in a small size machine. Because of

the poor absorption by thermal ions, the cavity modes may become prominent and radiation losses are enhanced. The presence of the fast ions plays the similar role as the hot minority species generated by ICRF itself if the beam fast ion is injected perpendicularly to B_o. As seen from Fig. 13, the absorbed power spectra broadens and the cavity effect is suppressed if the fast ions are present. In ASDEX experiment[21], indeed, the better absorption has been found in the heating scheme of NBI+ICRF ($2\Omega_H$) than the case $2\Omega_H$ alone.

One example[14,27] can be examined in a case of combined minority heating D(H), and the NBI($D^o \rightarrow D^+$). Only the perpendicular beam component of deuterons may act as the same role as the minority does in their second harmonic resonance ($\Omega_H = 2\Omega_D$). The question is how the absorbed energy distributes among the minority H and the beam components of D. We study the direct absorption rate and the partition rate by using the wave-code. In Fig. 18(a), we plot the partition ratio of the direct absorption for the case of (D^o(45 keV)$\rightarrow D^+$) + (D(H);33.5 MHz). The minority ratio is fixed to be 5% (n_H/n_e=5%) and the absorption rate is plotted versus the density of the beam component. The total absorption is little affected by the presence of the beam component, even if we simulate the beam component to be isotropic. If we consider the actual injection angle of the NB in ASDEX experiment, the calculated values in Fig. 18(a) correspond to the case where the perpendicular component is over-estimated. Provided that most of the power, which is absorbed by the minority H and the beam of D, is transferred to electrons, the presence of the beam affects the power partition ratio little. Compare the values of the power input to bulk deuterons, D_c, for different concentration ratio of the beam component.

It should be compared with the case of (H^o(42 keV)$\rightarrow H^+$) + (Ω_{2H}; 67MHz), the results are shown in Fig. 18(b). In order to examine a catalytic effect of the beam in an actual situation, we introduce an anisotropy ($T_\perp$ = 10 keV and $T_{\parallel}$ = 30 keV) of the beam component. Owing to the high energy, the beam component acts as a catalyst to transfer the absorbed energy to electrons through collisions like the high energy tail of the minority in minority heating scheme. As seen in Fig. 18(b), the power absorption by the beam component is about 10% for the parameter of n_{hot}/n_e=2%. If we again consider the collisional transfers and assume that the power absorbed by the beam component is almost completely transferred

to electrons, the presence of the beam changes the power partition such as to increase P_{et}/P_{abs} about 10% as much. We have a qualitative agreement with the experimental observations. The studies on the transport are left for the future.

§5 Effect on Peripheral Plasma Region

In this section, we discuss the possible effects of ICRF wave launching on the peripheral region of the plasma. Firstly, we consider a possible origin of impurity influx due to the strong reactive field in front of the antenna[23]. This affects the radiation in the plasma and may cause the power loss $\bar{P}_{NON}$ in Eq.(5). We next consider the effect of the throat into the divertor chamber. There is a possibility that the divertor throat could play a role of a hole in the wall allowing the launched ICRF waves to escape and be damped in divertor chamber[5]. If this part of the chamber can be regarded as a perfectly reflecting boundary for the wave, this effect is negligible.

Let us start with the possible origin of the impurity influx. We show the reactive electric field along the z-direction on the magnetic surface of the antenna location in Fig. 9(a) (imaginary part). The reactive field usually does not contribute to the power input to the plasma. However, this strong electric field directly affects the motion of ions in the scrape-off layer and might cause some sputtering of impurities. The ExB drift velocity of the ion, v_E, is estimated to be

$$v_E^2 = \frac{\Omega_I^2(\omega^2 + \Omega_I^2)}{(\omega^2 - \Omega_I^2)^2} \cdot \frac{E^2}{B^2} \qquad (11)$$

where Ω_I is the cyclotron frequency of the ions of the interest. This relation shows two possible mechanisms to enhance the energy of ions near the antenna. One is due to the resonance of $\omega \sim \Omega_I$. Usually this condition is not satisfied in a scrape-off layer near the antenna. Another is due to the strong field near the antenna, the maximum value of which is of the order of

$$E = C\sqrt{2/\hat{R}}(\hat{X}/L_A)\sqrt{P} \qquad (12)$$

(assuming that $\hat{X} \gg \hat{R}$). The coefficient C denotes the effect of the inhomogeneity of E_y along the antenna, which must be evaluated by the two dimensional calculation. C usually ranges up to 2.5 for the plasma with $a_s \simeq 0.4$ m[23]. We, in the following, give a heuristic argument on the effects of the reactive field. If one takes the typical value of Z for ASDEX as $\hat{R} \simeq 5\Omega$ and $\hat{X} \simeq 50\Omega$, the maximum value is estimated as

$$\bar{K}_{max}(eV) \simeq 10^{-4} P(W) + T_I(eV) \qquad (13)$$

where T_I is the average energy in the absence of the wave field.
This implies that $\bar{K}_{max}$ exceeds 100 eV at the power level of 1 MW, even if $T_I=0$. The sputtering yield ratio $Y(v_I)$ becomes greater than 10^{-3} for $\bar{K}>120$ eV in the case of H^+ collision on the iron surface[24]. Since the function $Y(v_I)$ shows a strong energy dependence near this energy, the power which corresponds to $\bar{K} \simeq 100$ eV can be considered to be a threshold power. We define the threshold rf power in this meaning.

The ion impurity source from the antenna is estimated to be $\bar{n}_s Y v_I$, where $\bar{n}_s$ is the number density of the scrape-off plasma and v_I is the incident velocity. The effective area which contributes to the sputtering is approximated by $S \sim a_L(b-a_L)L_T/d$. We use this value instead of the value $S \sim L_T L_A$, since we assume the localization of the strong electric field in poloidal direction. The total rate of the impurity source per unit time, Γ, may then be estimated as

$$\Gamma \sim 2Y(v_I)\bar{n}_s v_I \frac{a_L(b-a_L)}{d} L_T \quad \text{(atoms/sec)}. \qquad (14)$$

At the power level of 1MW, Eq.(16) gives the maximum energy of $\bar{K}_{max} \simeq 100$ eV and the incident velocity $v_I \sim 10^5$ m/s. For this energy, $Y(v_I)$ is ealuated to be 10^{-3}. We here note that $\bar{K}$ reaches 100 eV at lower rf power if $T_I \neq 0$ holds. Substituting the geometrical parameters, we have the source of iron impurity as $\Gamma \simeq 3\,\bar{n}_s$ (atoms/sec; $\bar{n}_s$ is measured in m^{-3}). For the higher power case, say P=2 MW, $\bar{K}_{max} \simeq 200$ eV and $v_\perp \simeq 1.4 \times 10^5$ m/s hold. $Y(v_I)$ is higher for this case $Y \simeq 5 \times 10^{-3}$. The source is estimated to be $\Gamma \simeq 20\,\bar{n}_s$ (atoms/sec). In the experiments of ASDEX, $\bar{n}_{sH} \leq 10^{18}$ m^{-3}. In the absence of ICRF launching, the measurement of the impurity confinement time, τ_I, is estimated to be 2~ 5msec. (The screening effect of SOL plasma is taken into account.) The impurity density in the stationary state, $n_I \sim \Gamma \cdot \tau_I / V_p$ (V_p: plasma volume), is estimated to be $\sim 10^{16}/m^3$ for the parameter of $P_{abs} \sim 2$ MW, $T_I=0$, and $\bar{n}_{sH} \simeq 10^{18}$ m^{-3}. This value of n_I would

give rise to a radiation loss in the plasma. This loss might be related to the enhancement of the radiation loss during the ICRF heating. In the ASDEX experiments without the wall carbonization, the central radiation loss is of the order of 50 kW/m^3 per MW of ohmic heating power (OH plasma) and of 120-160 kW/m^3 per MW of total heating power (ICRF plasma). The estimate of n_I given here is the crude evaluation. The value is within the experimental observations[25,26]. More precise study is necessary for the quantitative comparison.

The different feature of the electric field is seen in the case of the 2nd harmonic heating case. The loading resistance is a little larger than that of the minority heating case, but the maximum electric field is higher due to the large reactance. The field does not localize to an antenna as seen from Fig. 9(b). Taking into account this process, we may say that the threshold power to release the impurity becomes lower than the minority case and that, if it exceeds the threshold, then the impurity influx can be larger because of the larger area of the impurity source.

As for the direct loss of rf power from the chamber, we consider a possiblity that the wave escapes from the divertor throat area and is absorbed in the divertor chamber. This loss may become noticeable if the cavity eigenmode is strongly excited. The loss has been estimated in a crude manner in Ref. /5/. For cavity eigenmodes the wave field has a coherent structure in the toroidal and poloidal directions. The wave field can leak either from ports or throats. The loss rate is estimated, assuming that the wave leaks into unbounded space, as

$$\frac{P_{loss}}{P_{rf}} \simeq \frac{r_n^2}{12\pi d^2} \times \frac{\hat{R}^2 + \hat{X}^2}{\omega \mu_o (b-d)\hat{R}} \times (kr_h)^2 \exp(-2l\Delta k_{\parallel}) \qquad (15)$$

where r_h is the measure of the width in the poloidal direction of the throat, k is the vacuum wave number, $\Delta k_{\parallel}$ is the width of the cavity resonance, and l is the antenna throat distance. According to this calculation, in ASDEX, the loss from the throat may reach 5% at most. This estimate is the upper bound of the loss through the throat, because the wave is assumed to be not reflected back from the divertor region and we evaluate $\exp(-2l\Delta k_{\parallel}) \sim 1$. We also note that this loss becomes smaller when the coupling and absorption becomes large in the high density and high temperature target plasma.

§6 Summary and Discussion

In this report, we examined the ICRF propagation, absorption structure and coupling to the ASDEX plasma. The absorption structures are combined to the Fokker-Planck analysis. The temporal evolution of the heating structures are also obtained.

The coupling studies were applied to both the minority heating scheme and the 2nd harmonic resonance heating scheme. The accessibiity of the wave and the total loading impedance were examined for different experimental conditions. The global loading change in the L/H transition is simulated. The analysis fairly agrees to the experimental observations[17]. Present launching condition is found to be chosen in the range of an optimum loading condition.

In the minority heating case, the major part of the wave power is absorbed by the minority ion species. Therefore, the wave generates the high energy ions in the core region. These fast ions transfer the wave power to both electrons and bulk deuterons due to the collisional processes. Our analysis shows that more than 70% of the absorbed wave power is used to heat electrons at the power level of 0.5 MW (central heating case): And the fast ion energy reaches 40 keV. The parametrical dependences were also examined. We compared the cases of the central deposition and off-central deposition.

In addition to the analysis of the heating process, we examined the effect of the global wave field in the scrape-off layer. The role of the reactive electric field associated with the wave launching is discussed. This field might be a candidate to cause an impurity influx from the antenna region. The rough estimation was done for the ASDEX experiment. The analysis shows that the impurity sputtering might become noticeable at the power level of $\simeq$1 MW. The additional impurity influx can induce an enhancement of the impurity radiation. The loss rate becomes an appreciable amount in the case of the high power experiments. In order to reduce the impurity influx, both the increment of the loading resistance and the reduction of the antenna reactance as well as the reduction of the density of the scrape-off plasma in front of the antenna (still keeping a good coupling to the plasma) would be necessary. Problems (how to realize) are left for future.

The direct loss rate through the divertor throat was roughly estimated. This loss may be appreciable when the cavity formation is realized in the plasma. The crude analysis tells us that the case of the 2nd harmonic heating (without NBI) has a more severe loss than the case of the minority heating.

In this article, we do not take into account the spatial transport losses. The spatial loss affects the heating structure and, at the same time, the heating affects the spatial loss. One of the prominent features in the spatial loss in the ICRF heating process is the loss of the generated fast ions. Even if we do not consider the anomalous transport due to fluctuations, we may have an enhanced diffusion of fast ions. Namely, if we consider the neoclassical diffusion of ions, such as the plateau ($D_p \propto v^3$) and the ripple-trapped ($D_r, \propto v^7$) diffusions, it has velocity dependences. The particles of the higher kinetic energy escape faster than the thermal ions. The minority heating generates the fast ion tail component, and the tail energy increases as the heating density ξ increases. We have examined the loss rate of the fast ions by the model analysis[27, 28]. We have found that if the value of ξ exceeds a certain critical value, the loss rate becomes noticable compared with the heating power. This implies that 1) the effective heating rate decreases as the heating density increases and that 2) the loss of the fast ions becomes large. If the value of $\xi \simeq P_{rf}\tau_s/n_H T_e$ exceeds 30, then these effects can be seen. The present ASDEX ICRF experiment is in the range of the average value $\bar{\xi} \simeq 8$ (for $P_{rf} \simeq 2$ MW, τ_s is slowing-down time of fast ions ~20 ms, $\bar{n}_H \simeq 1.5 \times 10^{18}$ cm^{-3}, $\bar{T}_e \simeq 2$ keV, $V_p \sim 5$m^3). Our analysis in §4 (Fig. 11(b) for example) shows that the local value of ξ reaches 20-30 in the present experimental conditions. The knowledge of the confinement characteristics of fast ions is a key issue for the burning plasma and for the enhancement of the fusion cross-section.

As was calculated in §4, the fast ion tail is formed in accordance with the rise of the power to electrons. For the parameters of Fig. 10, it takes about 20 msec to see the appreciable amount of fast ions from the onset of ICRF. In the plasma periphery, the fast ions are observed in ASDEX experiment right after the onset of ICRF[29]. These fast ions may be accelerated by the other mechanisms than that discussed in this report.

The comprehensive study in experiments is necessary and is left for future work.

Acknowledgement

The authors would like to acknowledge Dr. F. Wagner, Dr. M. Brambilla for elucidating discussions, critical reading of the manuscript and the hospitality, Prof. M. Porkolab, Dr. G. Fussmann and Dr. F. Wenser for stimulating discussions. Two of the authors (S.I.I. and K.I.) acknowledge Mr. J.Kisslinger and Mrs. I. Ott for help in computations, members of the ASDEX group and Dr. H. Wobig for the hospitality. They also thank Mrs. R. Thormählen and Miss C. Weller for kind helps during their stay at IPP Garching.

Computations are performed by using the CRAY-computer in the Computer Center of the Max-Planck-Institut für Plasmaphysik.

Work is partially supported by Grant-in-Aid for Fusion Research and Grant-in-Aid for Scientific Research of Ministry of Education, Japan.

Table 1

Major radius	$R = 1.67$ m
Minor radius (at separatrix)	$a_s = 0.4$ m
Guard limiter location of an antenna	$a_L = 0.43$ m
Antenna location	$d = 0.45$ m
Wall location	$b = 0.51$ m
Magnetic field	$B_o = 2.24$ T (central heating) 2.4 T (off-central heating)
Electron density at center	$n_e(o) = 5 \times 10^{19}$ m^{-3}
RF frequency	$\omega/2\pi = 33.5$ MHz (minority ion heating) 67 MHz (2nd cyclotron heating)
Majority ion species	deuteron (minority ion heating) hydrogen (2nd cyclotron heating)
Minority ion species	hydrogen
Antenna width	$L_T = 0.18$ m
Antenna arc length	$L_A = 0.78$ m
Scrape-off density	$n_{se} = 10^{19}$ m^{-3} (at separatrix)
Scrape-off temperature	$T_{se} = 100$ eV (")
Density fall-off length	$\lambda_n = 0.02$ m
Temperature fall-off length	$\lambda_T = 0.02$ m

References

1) B.D. McVey, Nucl. Fusion 19 (1979) 461.
2) M. Brambilla, Computer Physics Report 4 (1986) 71.
3) A. Fukuyama, S. Nishiyama, S.-I. Itoh and K. Itoh, Nucl. Fusion 23 (1983) 1005.
4) A. Fukuyama, K. Itoh and S.-I. Itoh, Computer Physics Report 4 (1986) 137.
5) K. Itoh, S.-I. Itoh and A. Fukuyama, Nucl. Fusion 14 (1984) 13.
6) K. Steinmetz and M. Brambilla, IPP report Garching IPP 4/219 (1984).
7) A. Mori, et al., Plasma Physics and Controlled Nuclear Fusion Research, Vol. 1 (IAEA London, 1984) p. 445.
8) J. Jacquinot, R. Anderson, D. Arbez, et al., in Plasma Physics and Controlled Fusion (Proc. 12th European Conf. Budapest, 1985), 28A (1986) 1.
9) S.-I. Itoh, K. Itoh and A. Fukuyama, Japanese Journal of Applied Physics 25 (1986) 1121.
10) K. Hamamatsu, Y. Kishomoto, M. Azumi, A. Fukuyama, S.-I. Itoh and K. Itoh, in Europhys. Conf. Abstr. 14th European Conference on Controlled Fusion and Plasma Physics (Madrid) Vol.3 (1987) p. 861.
11) T.H. Stix, Nucl. Fusion 15 (1975) 737.
12) T. Morishita, A. Fukuyama, K. Hamamatsu, S.-I. Itoh and K. Itoh, Nucl. Fusion in press.
13) S.-I. Itoh, A. Fukuyama, K. Itoh and K Nishikawa, J.Phys. Soc. Japan 54 (1985) 1808.
14) K. Steinmetz, M. Brambilla et al., in Europhys. Conf. Abstr. 14th European Conference on Controlled Fusion and Plasma Physics (Madrid) Vol. 3 (1987) p. 946.
15) J.-M. Noterdaeme, G. Janeschitz, K. McCormick, et al., ibid Vol. 2 (1987) p. 678.
16) P. Anderson, L.-G. Eriksson and M. Lisak, Nucl. Fusion 25 (1985) 175.
17) K. Steinmetz, Proc. 7th Topical Conf. on Application of Radio-Frequency Power to Plasmas, Kissimmee, USA, May 1987
18) A. Fukuyama, T. Morishita, Y. Kishimoto, K. Hamamatsu, S.-I. Itoh and K. Itoh, in Proceedings of 11th Int. Conf. on Plasma Physics and Controlled Nuclear Fusion Research (IAEA Kyoto, 1986) F-IV-1

and S.I. Itoh, K. Itoh, A. Fukuyama and T. Morishita, in Europhys. Conf. Abstr. 14th European Conference on Controlled Fusion and Plasma Physics (Madrid) Vol. 3 (1987) 1204.

19) K. Hamamatsu, private communication (1986).

20) S.-I. Itoh, A. Fukuyama and K. Itoh, Nucl. Fusion, 14 (1984) 224.

21) K. Steinmetz, G. Fussmann, O. Gruber et al., Plasma Physics and Controlled Fusion (Proc. 12th European Conf. Budapest, 1985), 28A (1986) 235.

22) K. Steinmetz, F. Wagner, F. Wesner et al., 13th European Conf. on Controlled Fusion and Plasma Heating, EPS, Schliersee Vol. 2 (1986) 21.

23) K. Itoh, A. Fukuyama and S.-I. Itoh, Comments Plasma Phys. Controlled Fusion, 10 (1986) 91.

24) J. Roth, J. Bohdansky and W. Ottenberger, IPP report Garching IPP 9/26 (1979).

25) G. Fussmann, et al., J. Nucl. Materials, 145-147 (1987) 96.

26) G. Fussmann, et al., 12th European Conf. on Controlled Fusion and Plasmas Physics, EPS, Budapest, Vol. 1 (1985) 195.

27) S.-I. Itoh and K. Itoh, in Proceedings of 11th Int. Conf. on Plasma Physics and Controlled Nuclear Fusion Research (IAEA) (Kyoto, 1986) E-III-5.

28) K. Itoh, S.-I. Itoh and A. Fukuyama, Research report of Institute for Fusion Theory, Hiroshima Univ., HIFT-131 (1987) "Effect of Ion Loss on ICRH Heating".

29) F. Ryter et al., 13th European Conf. on Controlled Fusion and Plasma Heating, EPS, Schliersee, Vol. 1 (1986) 101.

Figure Captions

Fig. 1 Illustration of the model geometry. $/x/=a_s$ denotes the separatrix radius. The scrape-off plasma extends to $/x/=a_L$. The region $a_L</x/\leq b$ is treated as vacuum. Antenna is located at x=d (low field side excitation) Wall position is $x=\pm b$.

Fig. 2 Procedure of the numerical calculation.

Fig. 3 Spatial structure of the wave for the case of minority heating. The x-dependencies of E_x and E_y on Z=0 plane are shown in (a) and (b). Solid lines for real part and dahsed lines for imaginary part. E_x component is the superposition of the fast wave and Bernstein wave (which is generated by the mode conversion). E_y component shows that the fast wave propagates into the plasma. The power deposition profile and Poynting flux are shown in (c). The integrated profiles, $\int P dz$ and $-\int S_x dz$ are shown. Resonance absorption by hydrogen and deuteron near the center, and the absorption by electron in the high-field side are illustrated. Cyclotron resonance surface is denoted by the arrow on the horizontal axis.
Parameters are: B=2.24 T, $\omega/2\pi$=33.5 MHz, a_s=0.4 m, a_L=0.43 m, d=0.45 m, b=0.51 m, $\lambda_n=\lambda_T$=0.02 m, L_T=0.18 m, $n_{oe}=5\times10^{19}$ m^{-3}, $n_{se}=10^{19}$ m^{-3}, T_{oe}=2 keV, T_{oi}=3 keV, T_{se}=0.2 keV, T_{si}=0.3 keV, n_H/n_e=0.05. Antenna is located on the low-field side and I_A=1A.

Fig. 4 $k_{\parallel}$-dependence of the loading resistance for the minority ion heating (parameters are the same as in Fig. 3). Thick solid line, thin solid line, dotted-dashed line and dotted line are for total absorption, absorptions by minority hydrogen, majority deuteron and electron, respectively. The $k_{\parallel}$ spectrum of the antenna current is also shown. Access of the shorter wave-length modes, $/k_{\parallel}R/\geq 25$, are limited by the vacuum between the antenna and plasma. Weak cavity resonances ($k_{\parallel}R \simeq$ 10, 15, 21, 25, 28 ...) are observed. Antenna current I_A is 1A. $\hat{R}$ = 8.2 Ω/m.

Fig. 5 Loading resistance $\hat{R}$ as a function of the fall-off-length in the scrape-off plasma ($\lambda_n=\lambda_T$). Line I is the standard case (Fig. 3). As the increase of the density at the edge of SOL, $n(a_L)$, the loading resistance increases. If $n(a_L)$ approaches the cut-off density of the local dispersion of the cold plasma, the λ_n dependence of $\hat{R}$ becomes weaker. Line II is the case of $d-a_L=3$ cm. The plasma-antenna distance is very effective to change the coupling. The line III indicates the case of higher edge density: $n_s=1.5\times10^{19}$ m^{-3}. Stronger dependence of $\hat{R}$ on λ_n is observed. Dotted lines indicate the case where antenna is far from the plasma: a_L-a_s = 5 cm. $d-a_L$ is also chosen to be 2 and 3 cm.

Fig. 6 Loading resistance ($\hat{R}$) and reactance ($\hat{X}$) as a function of the width of the antenna. When antenna width is wide, $L_T\cdot k_{\parallel c}\geq 2\pi$, R decreases with increasing L_T. In the narrow antenna limit, $L_T\cdot k_{\parallel c}<\pi$, $\hat{R}$ saturates while X continues to increase. Other parameters are the same as in Fig. 3. a_L-a_s = 3 cm (solid lines) and 5 cm (dashed lines). $d-a_L$ = 2 cm and 3 cm as indicated.

Fig. 7 $k_\parallel$ spectrum of the power absorption for the 2nd cycltoron resonance heating of pure hydrogen plasma. $n_e(0)=n_H(0)=5\times10^{19}$ m^{-3}, $n_s=10^{19}$ m^{-3}, $T_e(0)=2$ keV, $T_H(0)=3$ keV, $T_{es}=0.2$ keV, $T_{HS}=0.3$ keV, $\lambda_n=\lambda_T=2$ cm, $\omega/2\pi=67$ MHz and other geometrical paramters are the same as in Fig. 3. Due to the increase of the frequency, accessible range of the high $k_\parallel$ modes becomes wider compared to Fig. 4. The cavity mode is more prominent in this case due to the weaker damping than the case in Fig. 4. Power partition $\bar{P}_e/\bar{P}_{tot}=7.6\%$, and the total loading resistance per unit arc length is $\hat{R}\cong12.5$ Ω/m.

Fig. 8 Dependence of the loading resistance on λ_n and λ_T for the second cyclotron resonance heating of hydrogens. The stronger dependence is seen compared to the minority heating. Other parameters are the same as in Fig. 7. a_L-a_s = 3 cm (solid lines) and 5 cm (dashed lines). $d-a_L$ is indicated.

Fig. 9 The structure in the toroidal direction of the electric field (E_y on the plane x=d) is shown for the minority heating case (a: paramters are those in Fig. 3) and 2nd cyclotron heating case (b: paramters

are the same as in Fig. 7). Antenna center is located at Z=0. Strong reactive electric field is localized near the antenna. Half width of the antenna is 0.054 R. In the 2nd cyclotron heatin case, shorter-wave-length mode persists, reflecting the cavity components in Fig. 7. Solid lines for real component and dashed line for imaginary component.

Fig. 10 Temporal evolution of the heating powers to electrons and ions. Case of the central heating. Back-ground plasma parameters are $n_e(0)=5\times10^{19}$ m^{-3}, $n_e(a_s)=5\times10^{18}$ m^{-3}, $n_H/n_e=5\%$, $T_0=2$ keV, $T_s=0.2$ keV, $\omega/2\pi=33.5$ MHz, $B=2.24$ T, $\lambda_n=\lambda_T=0.02$ m, $L_y=0.2$ m and other geometrical paramters are the same as in Fig. 3. Total rf power is 0.15 MW.

Fig. 11 Power deposition profiles to electron and ion, and the radial temperature profile of the hot ion component in the steady state for central heating case. Low power case ($P_{rf}\approx0.16$ MW; a) and medium power case ($P_{rf}\simeq0.31$ MW; b). Half radius of ion-heating profile is wider compared to that of electron heating, parameters are those in Fig. 10.

Fig. 12 Ratio of the power partition as a function of the rf power. Ratio of the direct absorptions by electrons and ions (P_{ed}, P_{Dd}) and collisional transfer to electron and ions (P_{ec}, P_{Dc}) are shown. The thick line indicates the ratio of the electron heating. Parameters are the same as in Fig. 10. $P_{et}\simeq P_{Dt}$ holds around $P_{rf}\approx0.4$ MW.

Fig. 13 Change of the $k_{\parallel}$-spectrum of the power absorption as a result of the tail generation. Initial spectrum (dashed line) shows a cavity around $k_{\parallel}R\simeq6$, while in the final state (t=100 ms, solid line), the flatter spectrum is obtained. $P_{rf}\simeq0.3$ MW. Parameters are those in Fig. 10.

Fig. 14 a) Maximum value of the temperature of hot ion component as a function of the rf power (in the stationary state, t=50 ms). Solid line is for the central heating case (Fig. 10) and dashed line is for the off-central heating (see Fig. 15).

b) A plot of maximum tail temperature versus the value of the minority ratio $\eta' = n_H/n_D$ for the fixed power level.

Fig. 15 Example of the off central heating. B=2.4 T and P_{rf}=0.55 MW. Power deposition profile in the stationary state is shown. Other parameters are the same as in Fig. 10. By this change of the magnetic field, the resonance surface, $\omega=\Omega_H(x)$, moves to r/a_s=0.37. Because of the larger area of the magnetic surface, the power density averaged over the magnetic surface, for given P_{rf}, reduces compared to the central heating case.

Fig. 16 Temporal evolution of the heating power to electrons and ions after the onset of the rf power: off-central heating case (parameters are those in Fig. 15). Similar delay of the rise in P_{et} is observed as in Fig. 10.

Fig. 17 Power partition in the case of the off-central heating. Parameters are those in Fig. 15.

Fig. 18 The effect of the high energy component. The case of minority heating (a: other parameters are the same as in Fig. 3) and the case of the second cyclotron heating (b: see Fig. 7 for other parameters). T_h = 45 keV in (a) (isotropic) and $T_{\parallel}$ = 30 keV and $T_{\perp}$ = 10 keV in (b). Antenna current is chosen to be 1A; power per unit length of antenna is shown.

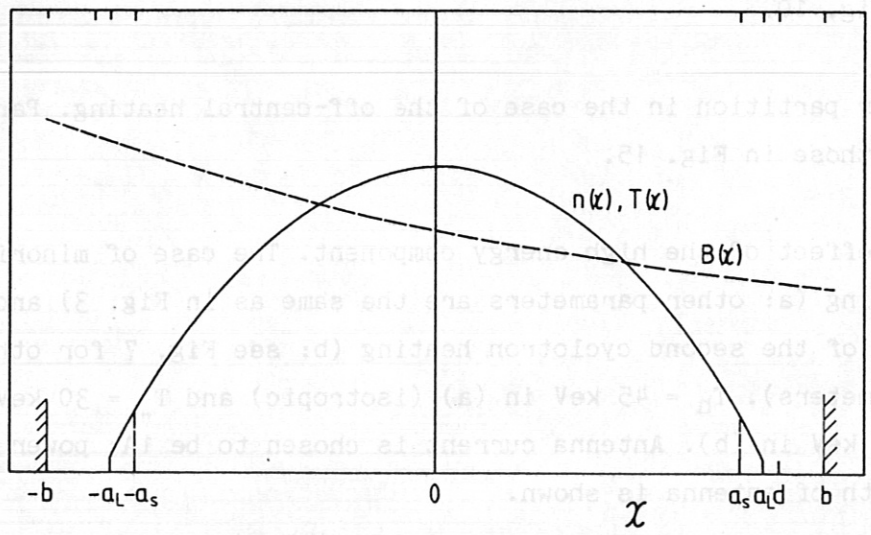

Fig. 1 Illustration of the model geometry. $/x/=a_s$ denotes the separatrix radius. The scrape-off plasma extends to $/x/=a_L$. The region $a_L < /x/ \leq b$ is treated as vacuum. Antenna is located at x=d (low field side excitation) Wall position is $x=\pm b$.

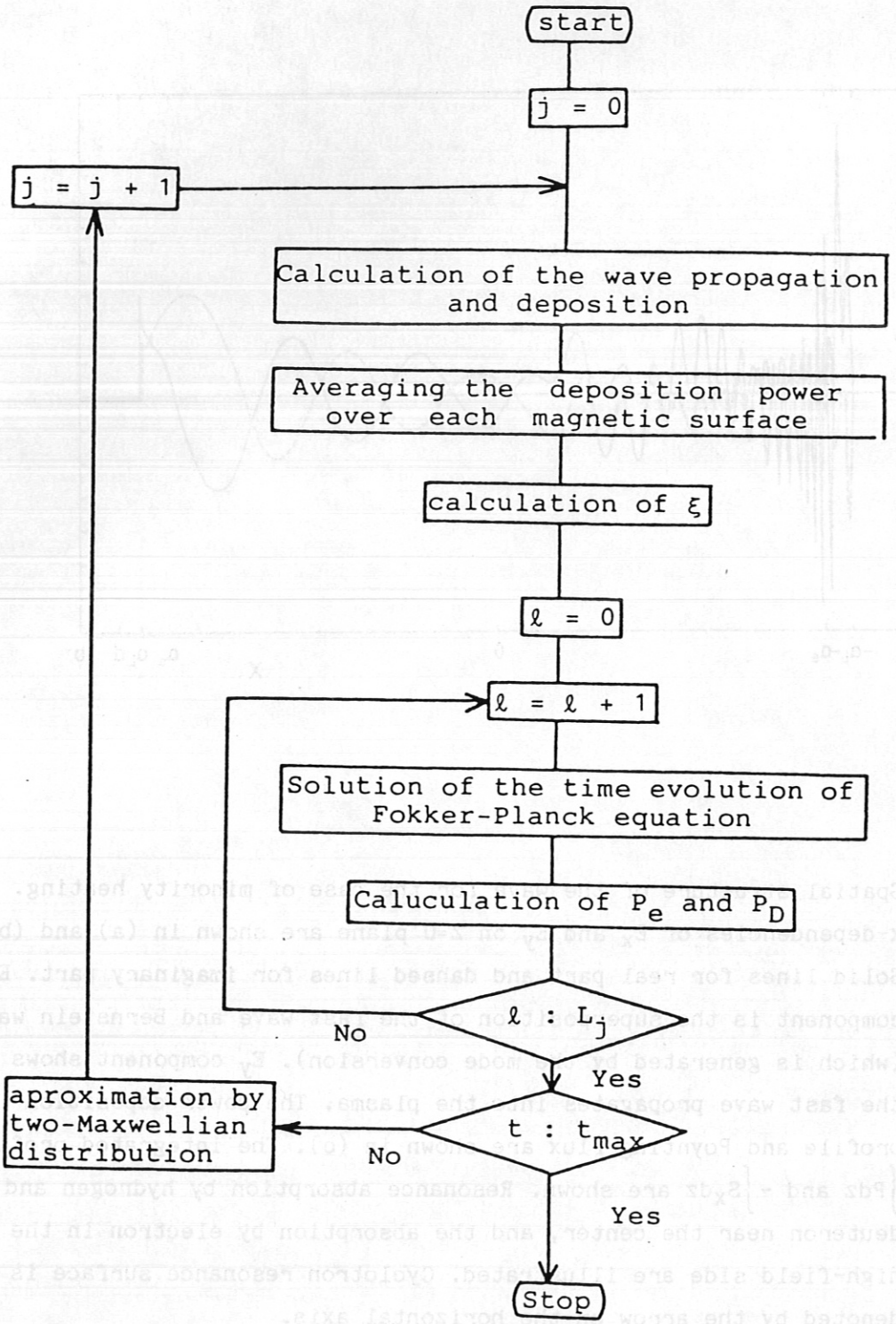

Fig. 2 Procedure of the numerical calculation.

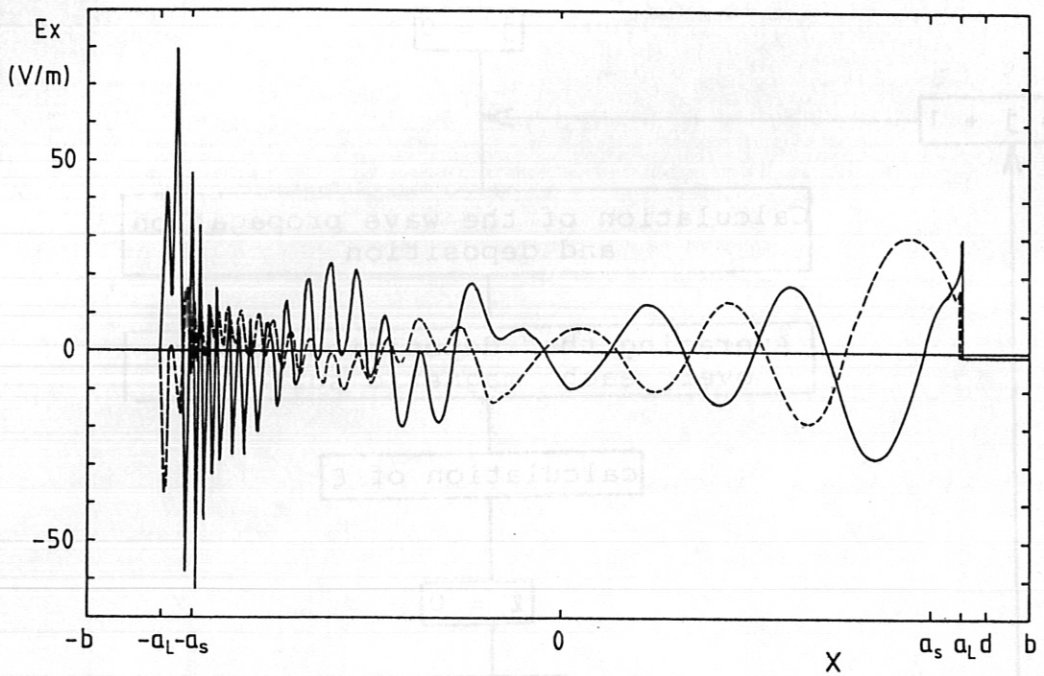

Fig. 3 Spatial structure of the wave for the case of minority heating. The x-dependencies of E_x and E_y on Z=0 plane are shown in (a) and (b). Solid lines for real part and dahsed lines for imaginary part. E_x component is the superposition of the fast wave and Bernstein wave (which is generated by the mode conversion). E_y component shows that the fast wave propagates into the plasma. The power deposition profile and Poynting flux are shown in (c). The integrated profiles, $\int P dz$ and $-\int S_x dz$ are shown. Resonance absorption by hydrogen and deuteron near the center, and the absorption by electron in the high-field side are illustrated. Cyclotron resonance surface is denoted by the arrow on the horizontal axis.

Parameters are: B=2.24 T, $\omega/2\pi$=33.5 MHz, a_s=0.4 m, a_L=0.43 m, d=0.45 m, b=0.51 m, $\lambda_n=\lambda_T$=0.02 m, L_T=0.18 m, $n_{oe}=5\times10^{19}$ m^{-3}, $n_{se}=10^{19}$ m^{-3}, T_{oe}=2 keV, T_{oi}=3 keV, T_{se}=0.2 keV, T_{si}=0.3 keV, n_H/n_e=0.05. Antenna is located on the low-field side and I_A=1A.

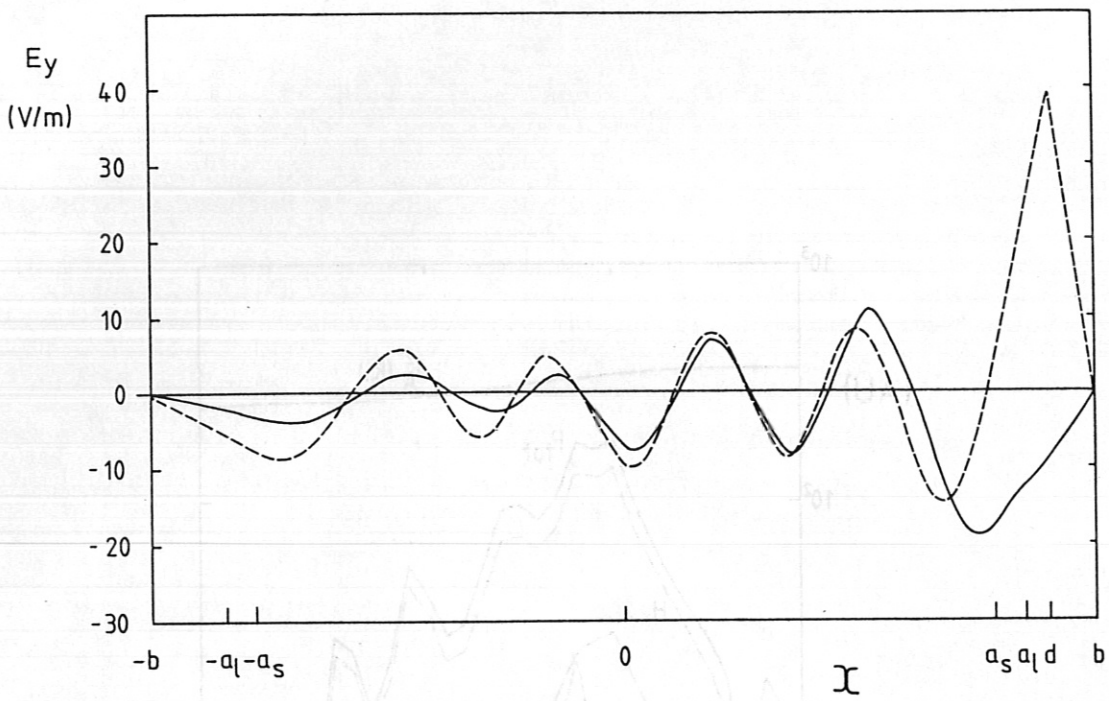
E_y
(V/m)
40
30
20
10
0
-10
-20
-30
-b
$-a_l-a_s$
0
a_s a_l d
b
x

Fig. 3(b)

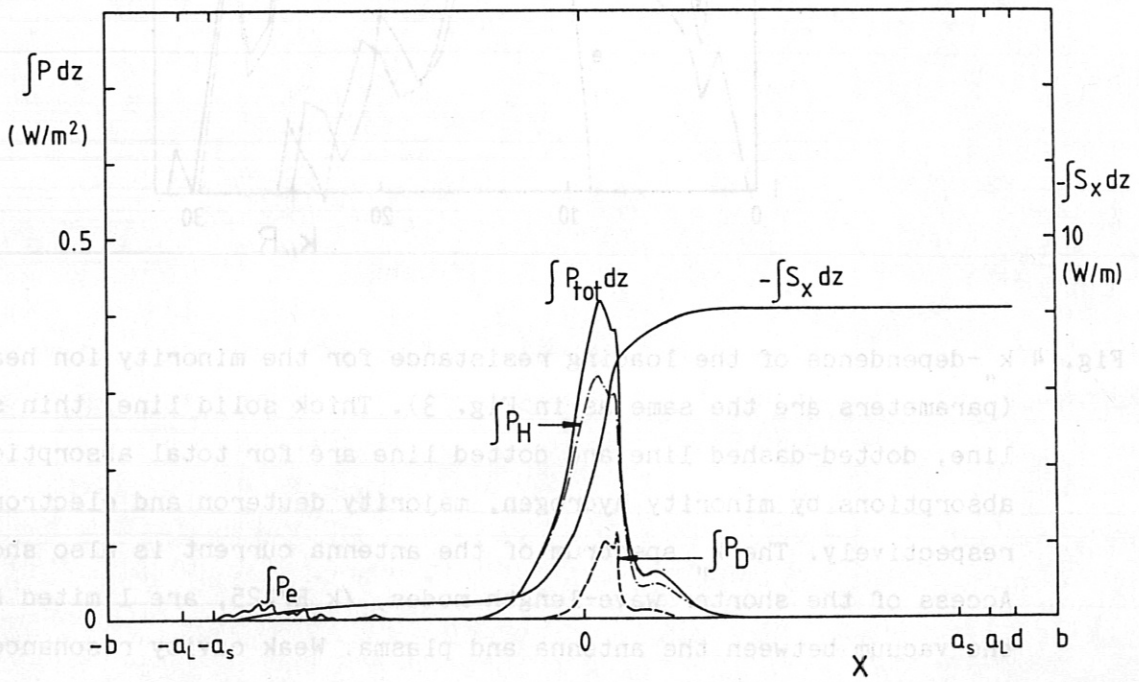
$\int P\,dz$
(W/m²)
0.5
0
$-\int S_x\,dz$
10
(W/m)
$\int P_{tot}\,dz$
$-\int S_x\,dz$
$\int P_H$
$\int P_D$
$\int P_e$
-b
$-a_L-a_s$
0
a_s a_L d
b
X

Fig. 3(c)

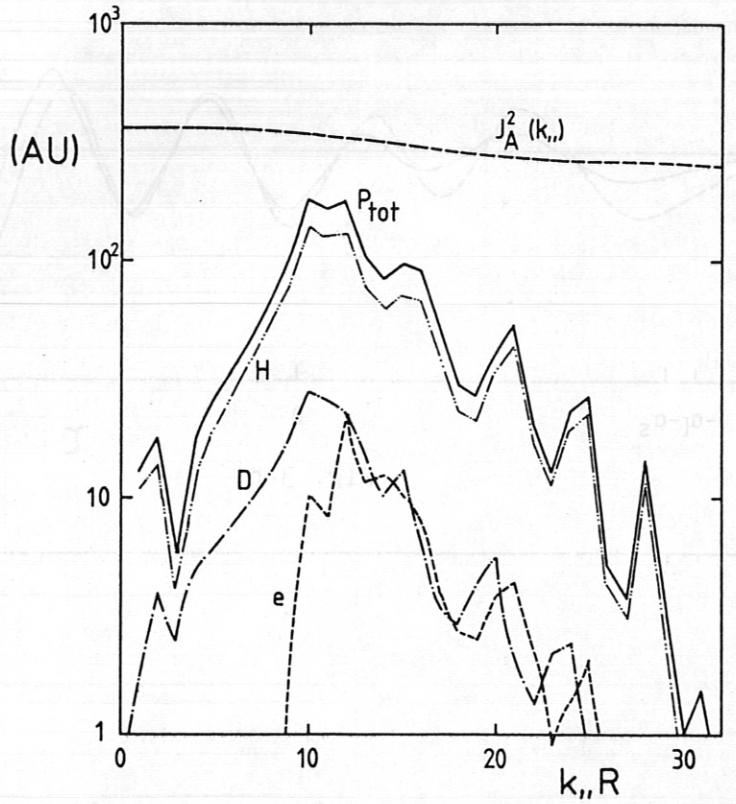

Fig. 4 $k_{\parallel}$-dependence of the loading resistance for the minority ion heating (parameters are the same as in Fig. 3). Thick solid line, thin solid line, dotted-dashed line and dotted line are for total absorption, absorptions by minority hydrogen, majority deuteron and electron, respectively. The $k_{\parallel}$ spectrum of the antenna current is also shown. Access of the shorter wave-length modes, $/k_{\parallel}R/ \geq 25$, are limited by the vacuum between the antenna and plasma. Weak cavity resonances ($k_{\parallel}R \simeq 10, 15, 21, 25, 28 \ldots$) are observed. Antenna current I_A is 1A. $\hat{R} = 8.2\ \Omega/m$.

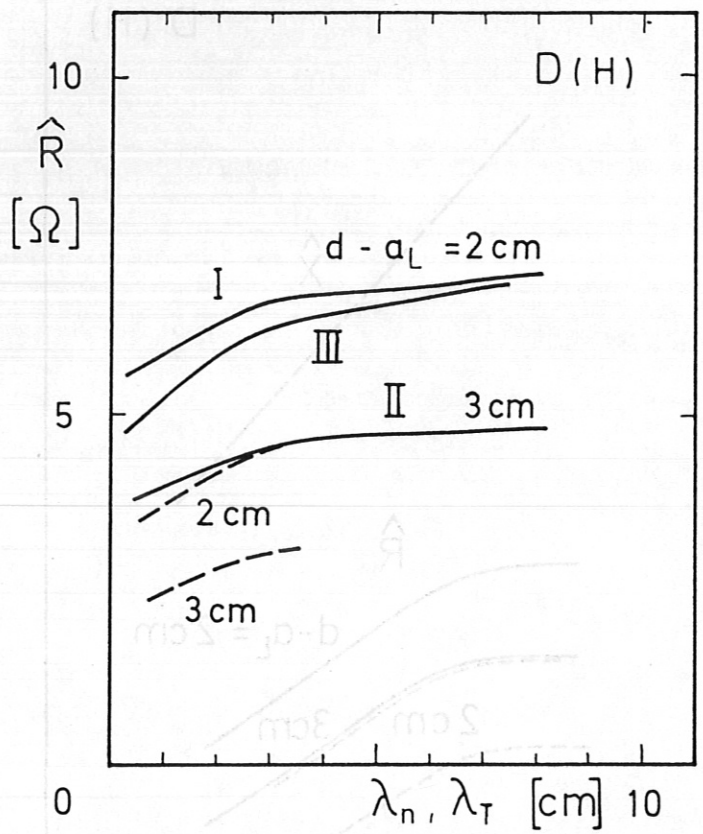

Fig. 5 Loading resistance $\hat{R}$ as a function of the fall-off-length in the scrape-off plasma ($\lambda_n=\lambda_T$). Line I is the standard case (Fig. 3). As the increase of the density at the edge of SOL, $n(a_L)$, the loading resistance increases. If $n(a_L)$ approaches the cut-off density of the local dispersion of the cold plasma, the λ_n dependence of $\hat{R}$ becomes weaker. Line II is the case of $d-a_L=3$ cm. The plasma-antenna distance is very effective to change the coupling. The line III indicates the case of higher edge density: $n_s=1.5\times10^{19}$ m^{-3}. Stronger dependence of $\hat{R}$ on λ_n is observed. Dotted lines indicate the case where antenna is far from the plasma: a_L-a_s = 5 cm. $d-a_L$ is also chosen to be 2 and 3 cm.

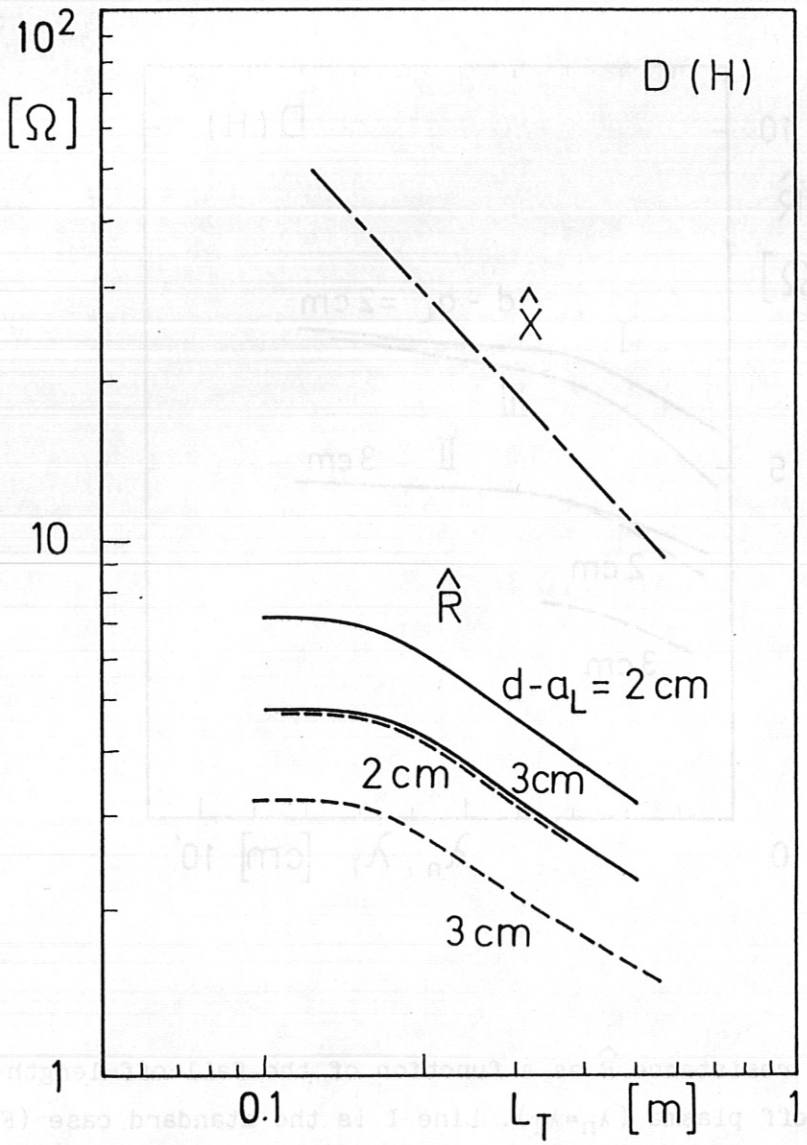

Fig. 6 Loading resistance ($\hat{R}$) and reactance ($\hat{X}$) as a function of the width of the antenna. When antenna width is wide, $L_T \cdot k_{"c} \geq 2\pi$, $\hat{R}$ decreases with increasing L_T. In the narrow antenna limit, $L_T \cdot k_{"c} < \pi$, $\hat{R}$ saturates while $\hat{X}$ continues to increase. Other parameters are the same as in Fig. 3. $a_L - a_s$ = 3 cm (solid lines) and 5 cm (dashed lines). $d-a_L$ = 2 cm and 3 cm as indicated.

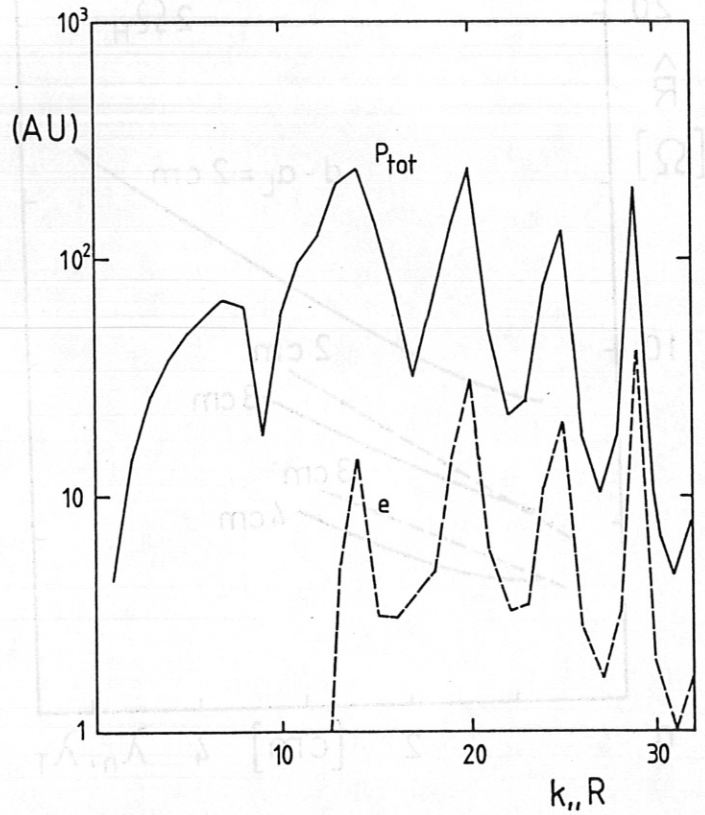

Fig. 7 $k_{\parallel}$ spectrum of the power absorption for the 2nd cycltoron resonance heating of pure hydrogen plasma. $n_e(0)=n_H(0)=5\times10^{19}$ m^{-3}, $n_s=10^{19}$ m^{-3}, $T_e(0)=2$ keV, $T_H(0)=3$ keV, $T_{es}=0.2$ keV, $T_{HS}=0.3$ keV, $\lambda_n=\lambda_T=2$ cm, $\omega/2\pi=67$ MHz and other geometrical paramters are the same as in Fig. 3. Due to the increase of the frequency, accessible range of the high $k_{\parallel}$ modes becomes wider compared to Fig. 4. The cavity mode is more prominent in this case due to the weaker damping than the case in Fig. 4. Power partition $\bar{P}_e/\bar{P}_{tot}=7.6\%$, and the total loading resistance per unit arc length is $\hat{R}\cong12.5$ Ω/m.

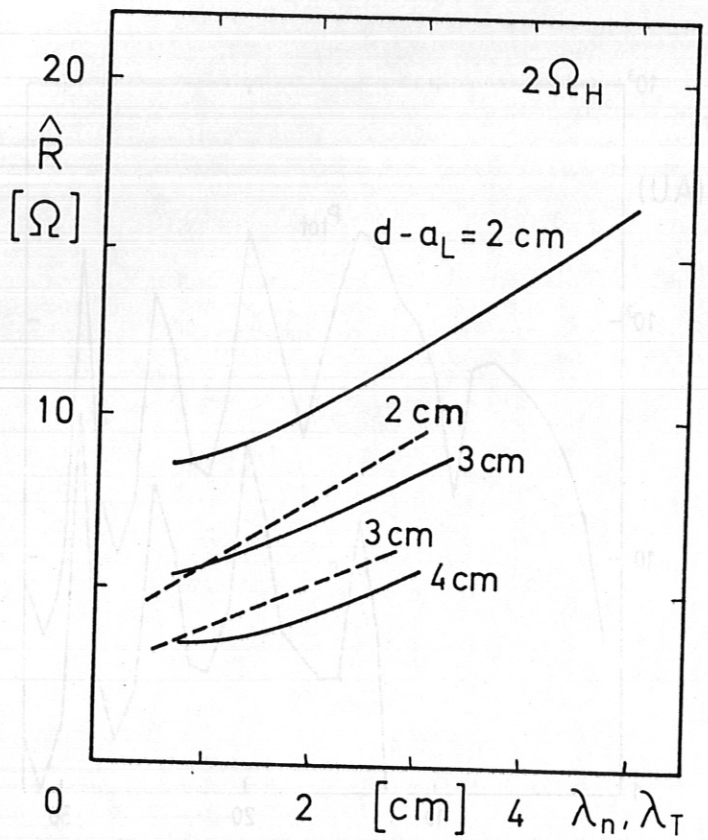

Fig. 8 Dependence of the loading resistance on λ_n and λ_T for the second cyclotron resonance heating of hydrogens. The stronger dependence is seen compared to the minority heating. Other parameters are the same as in Fig. 7. a_L-a_s = 3 cm (solid lines) and 5 cm (dashed lines). d-a_L is indicated.

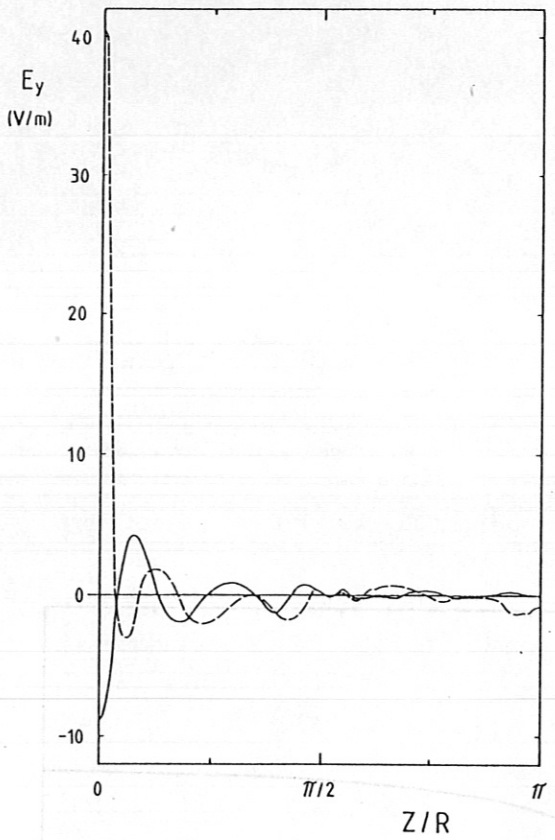

Fig. 9(a)

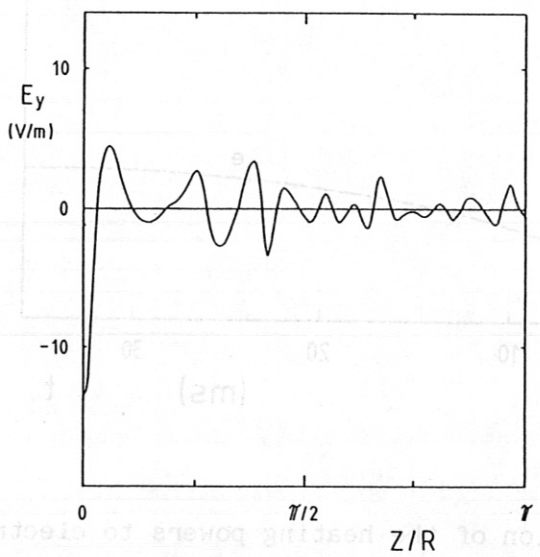

Fig. 9(b)

Fig. 9 The structure in the toroidal direction of the electric field (E_y on the plane x=d) is shown for the minority heating case (a: paramters are those in Fig. 3) and 2nd cyclotron heating case (b: paramters are the same as in Fig. 7). Antenna center is located at Z=0. Strong reactive electric field is localized near the antenna. Half width of the antenna is 0.054 R. In the 2nd cyclotron heatin case, shorter-wave-length mode persists, reflecting the cavity components in Fig. 7. Solid lines for real component and dashed line for imaginary component.

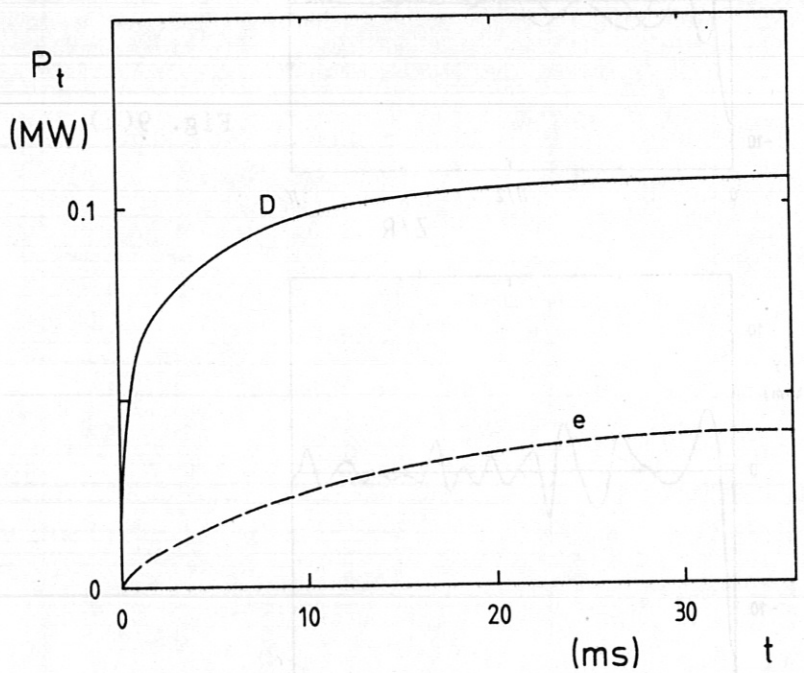

Fig. 10 Temporal evolution of the heating powers to electrons and ions. Case of the central heating. Back-ground plasma parameters are $n_e(0)=5\times10^{19}$ m^{-3}, $n_e(a_s)=5\times10^{18}$ m^{-3}, $n_H/n_e=5\%$, $T_O=2$ keV, $T_s=0.2$ keV, $\omega/2\pi=33.5$ MHz, B=2.24 T, $\lambda_n=\lambda_T=0.02$ m, $L_y=0.2$ m and other geometrical paramters are the same as in Fig. 3. Total rf power is 0.15 MW.

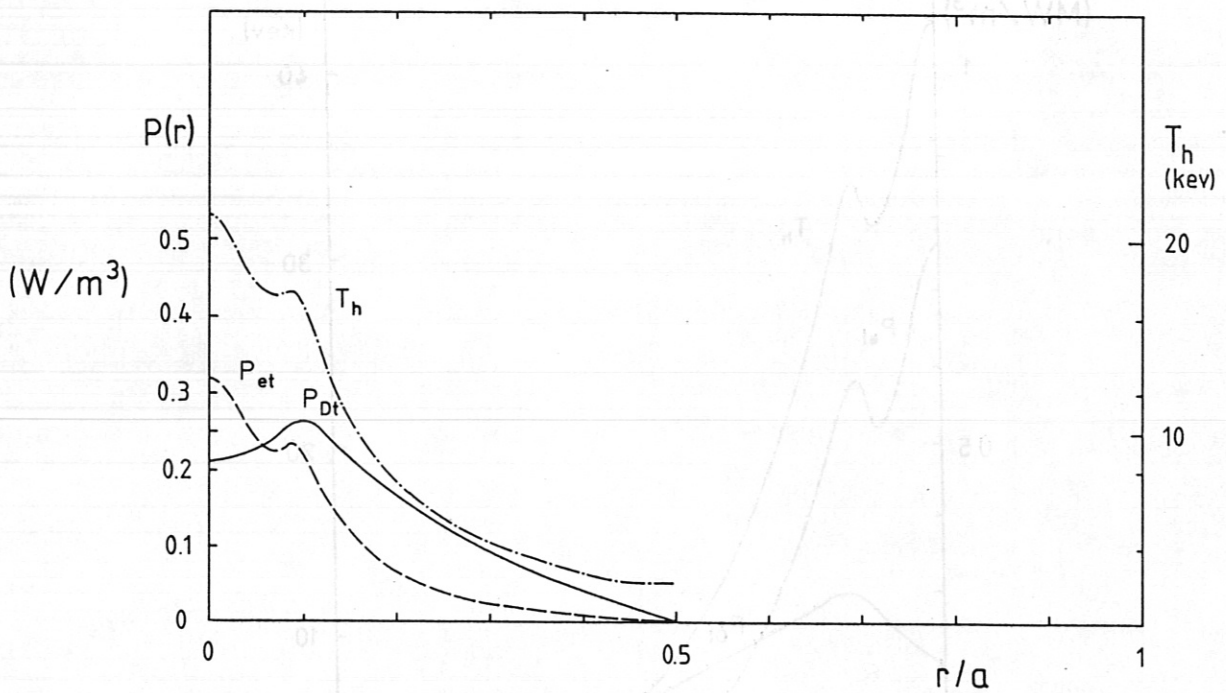

Fig. 11(a)

Fig. 11 Power deposition profiles to electron and ion, and the radial temperature profile of the hot ion component in the steady state for central heating case. Low power case ($P_{rf} \approx 0.16$ MW; a) and medium power case ($P_{rf} \approx 0.31$ MW; b). Half radius of ion-heating profile is wider compared to that of electron heating, parameters are those in Fig. 10.

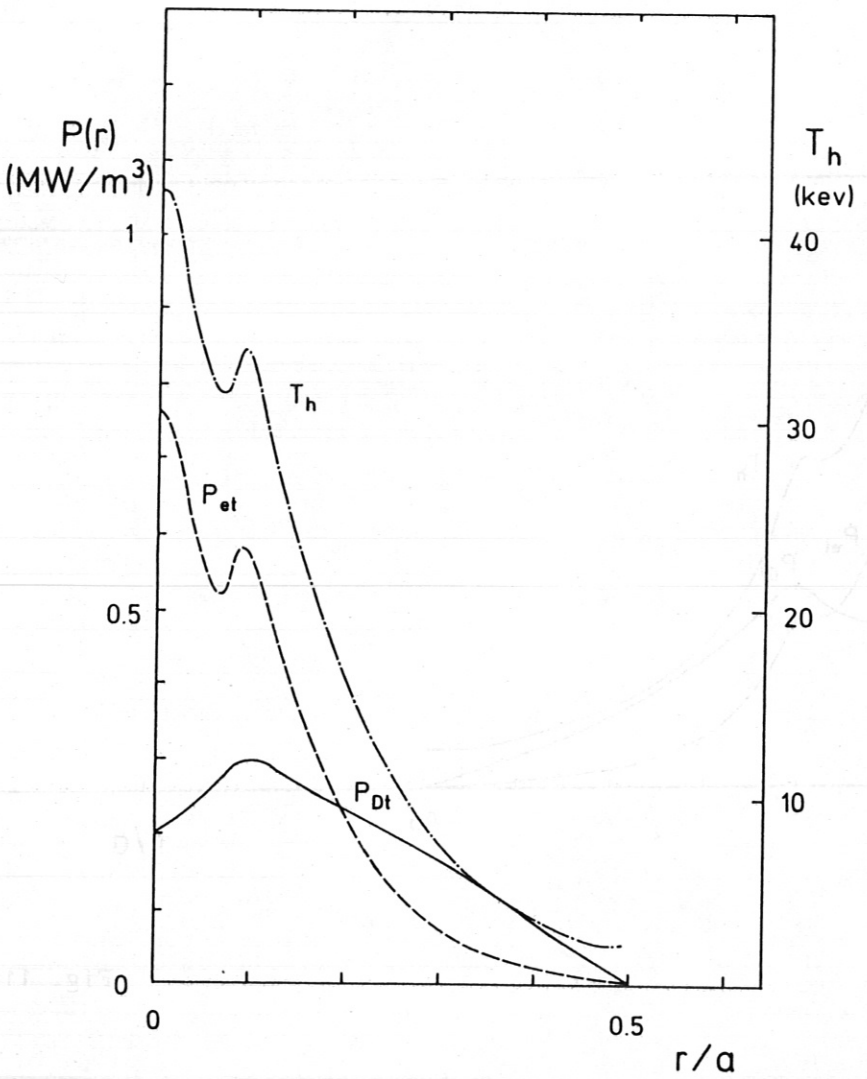

Fig. 11(b)

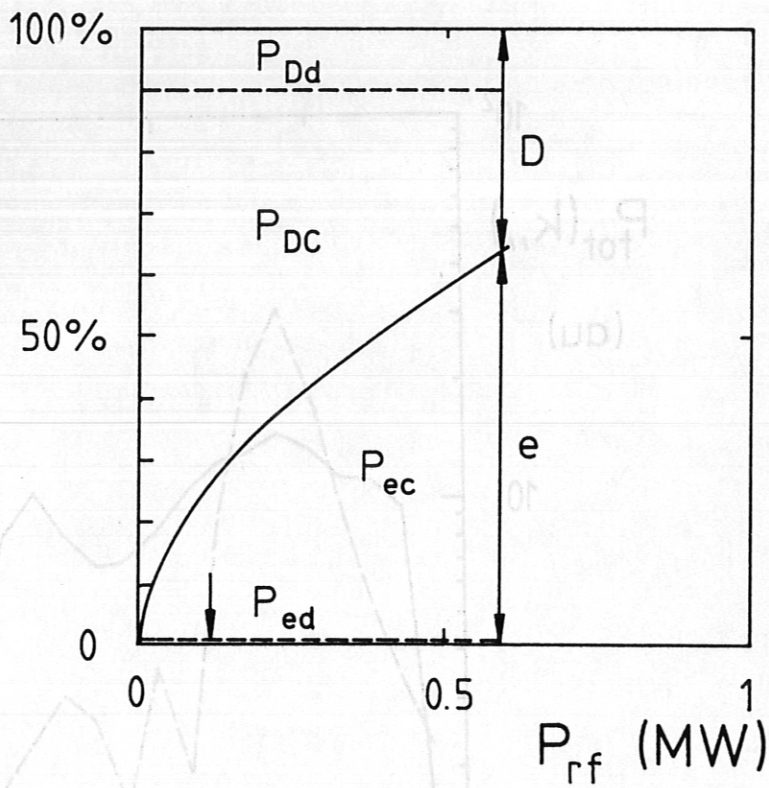

Fig. 12 Ratio of the power partition as a function of the rf power. Ratio of the direct absorptions by electrons and ions (P_{ed}, P_{Dd}) and collisional transfer to electron and ions (P_{ec}, P_{Dc}) are shown. The thick line indicates the ratio of the electron heating. Parameters are the same as in Fig. 10. $P_{et}=P_{Dt}$ holds around $P_{rf}\approx 0.4$ MW.

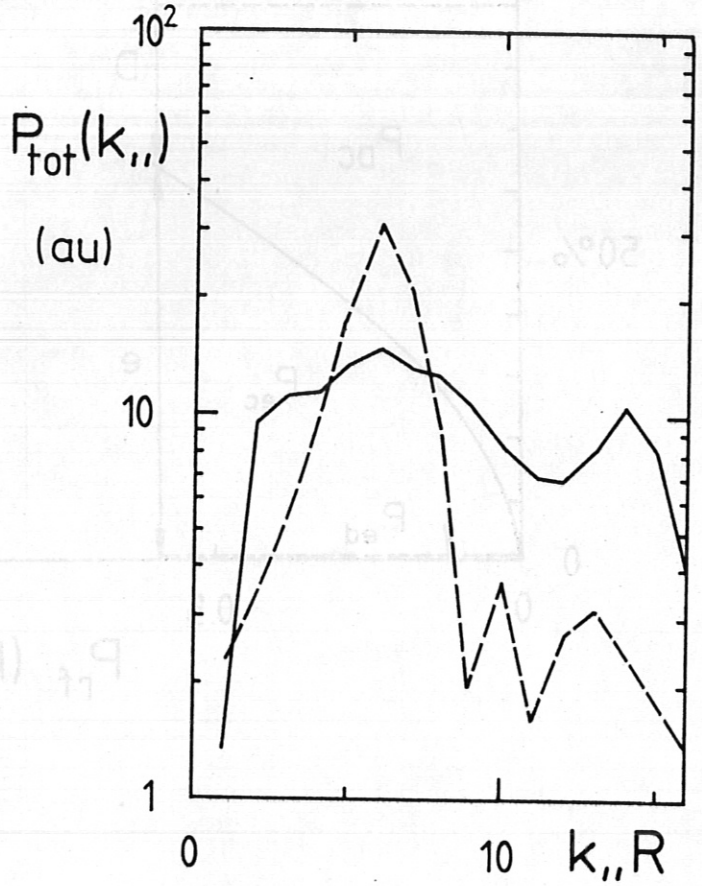

Fig. 13 Change of the $k_{\parallel}$-spectrum of the power absorption as a result of the tail generation. Initial spectrum (dashed line) shows a cavity around $k_{\parallel}R\approx 6$, while in the final state (t=100 ms, solid line), the flatter spectrum is obtained. $P_{rf}\approx 0.3$ MW. Parameters are those in Fig. 10.

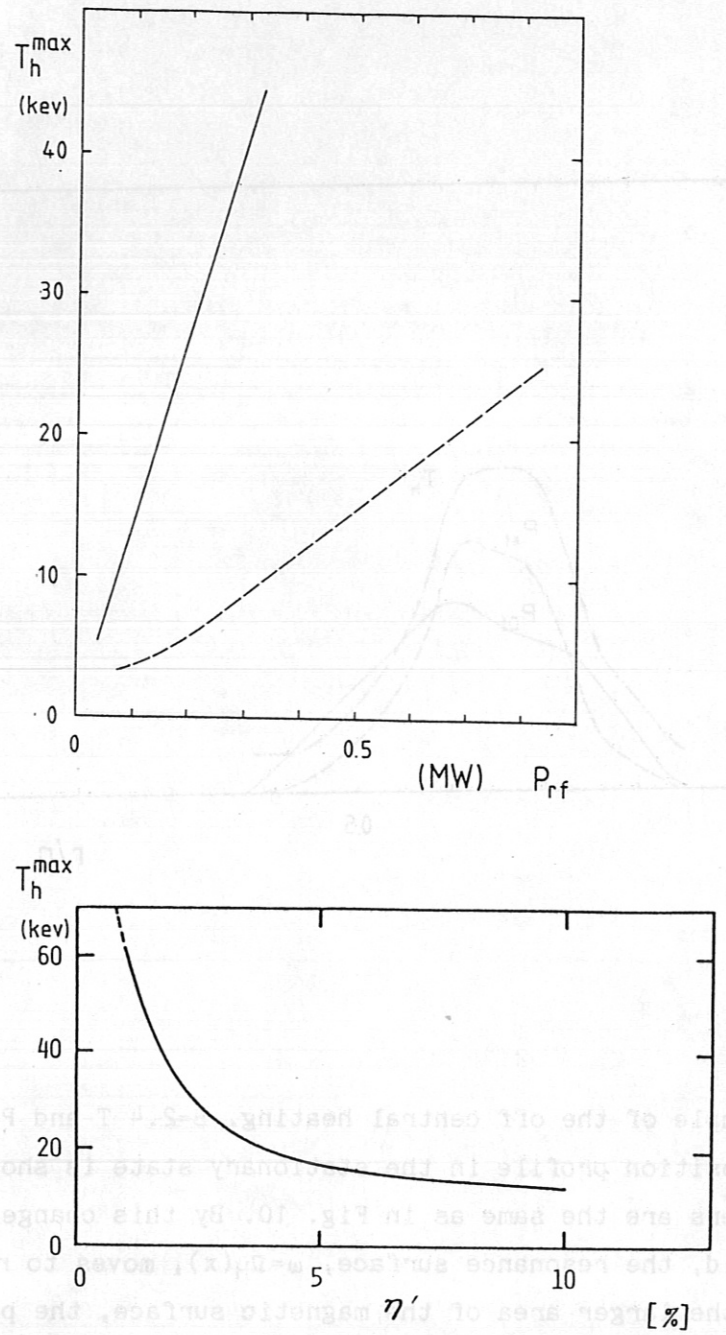

Fig. 14 a) Maximum value of the temperature of hot ion component as a function of the rf power (in the stationary state, t=50 ms). Solid line is for the central heating case (Fig. 10) and dashed line is for the off-central heating (see Fig. 15).

b) A plot of maximum tail temperature versus the value of the minority ratio $\eta' \equiv n_H/n_D$ for the fixed power level.

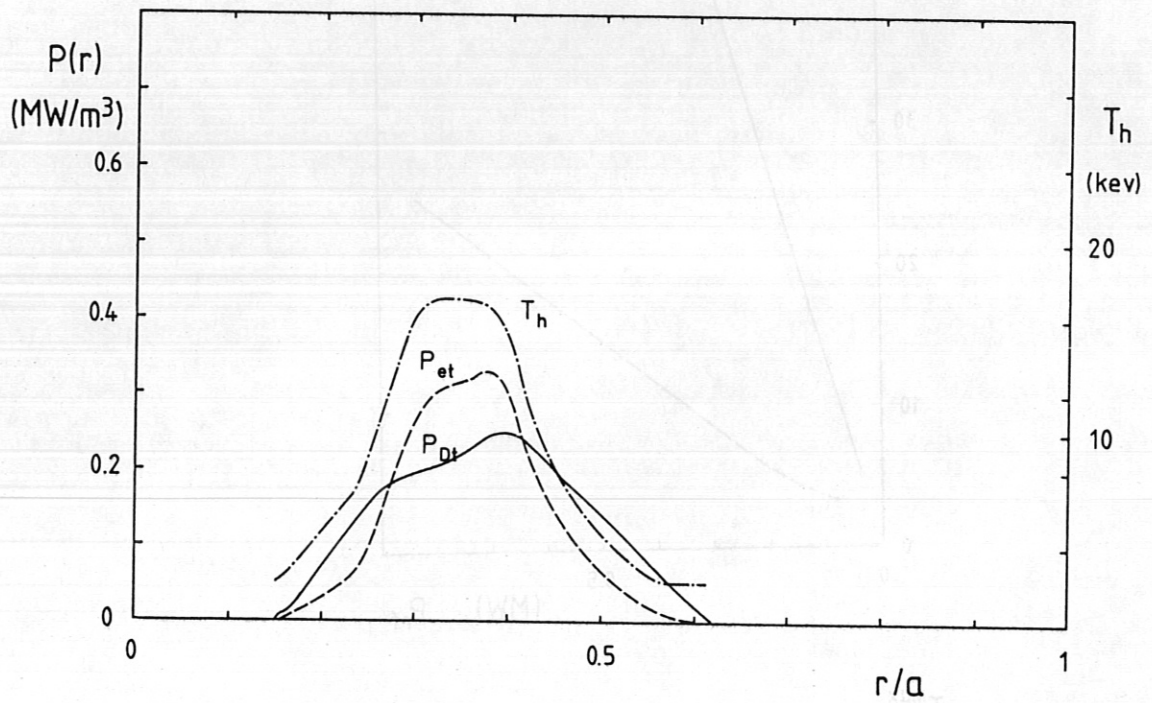

Fig. 15 Example of the off central heating. B=2.4 T and P_{rf}=0.55 MW. Power deposition profile in the stationary state is shown. Other parameters are the same as in Fig. 10. By this change of the magnetic field, the resonance surface, $\omega=\Omega_H(x)$, moves to r/a_s=0.37. Because of the larger area of the magnetic surface, the power density averaged over the magnetic surface, for given P_{rf}, reduces compared to the central heating case.

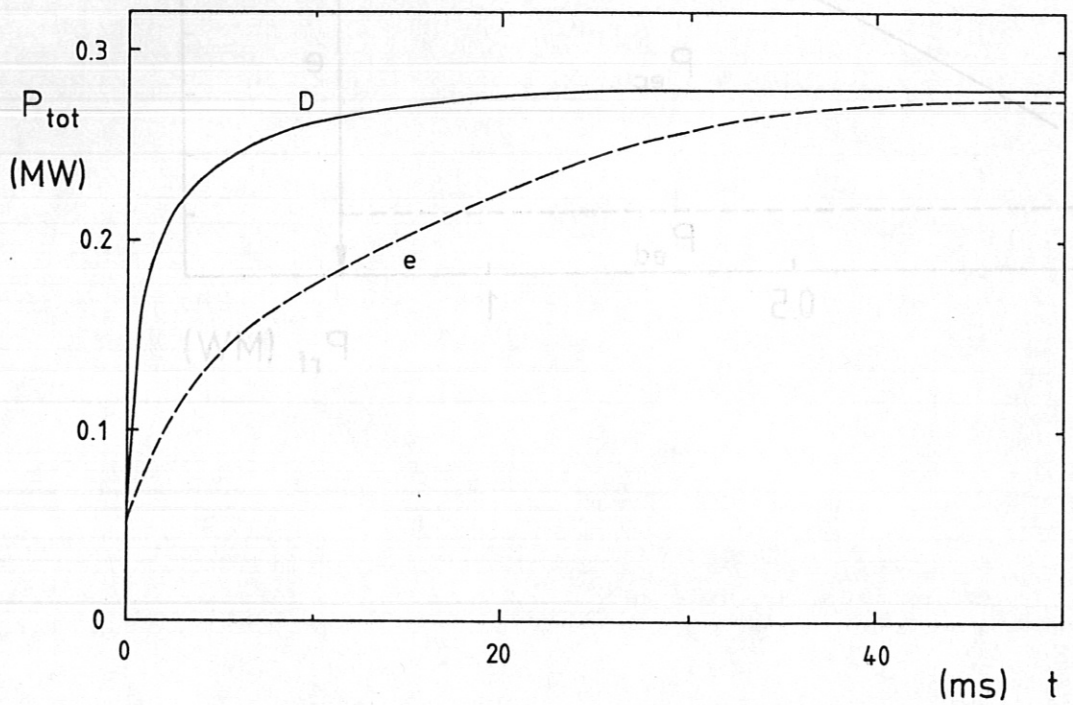

Fig. 16 Temporal evolution of the heating power to electrons and ions after the onset of the rf power: off-central heating case (parameters are those in Fig. 15). Similar delay of the rise in P_{et} is observed as in Fig. 10.

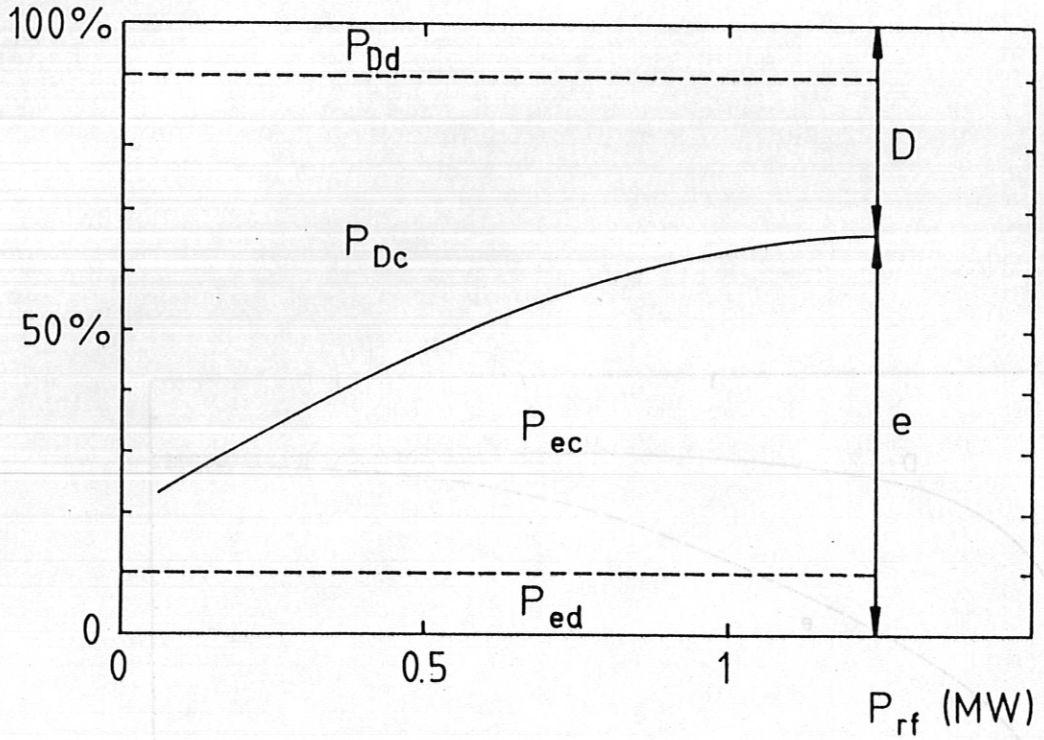

Fig. 17 Power partition in the case of the off-central heating. Parameters are those in Fig. 15.

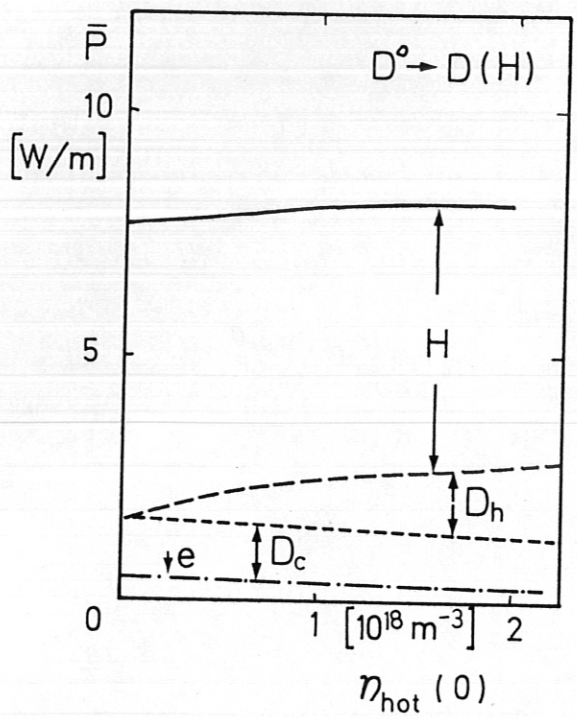

Fig. 18(a)

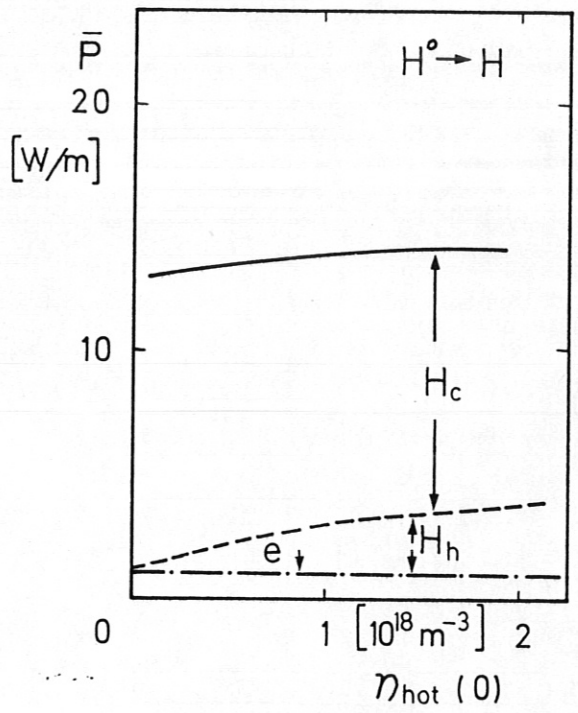

Fig. 18(b)

Fig. 18 The effect of the high energy component. The case of minority heating (a: other parameters are the same as in Fig. 3) and the case of the second cyclotron heating (b: see Fig. 7 for other parameters). T_h = 45 keV in (a) (isotropic) and $T_{\parallel}$ = 30 keV and $T_{\perp}$ = 10 keV in (b). Antenna current is chosen to be 1A; power per unit length of antenna is shown.